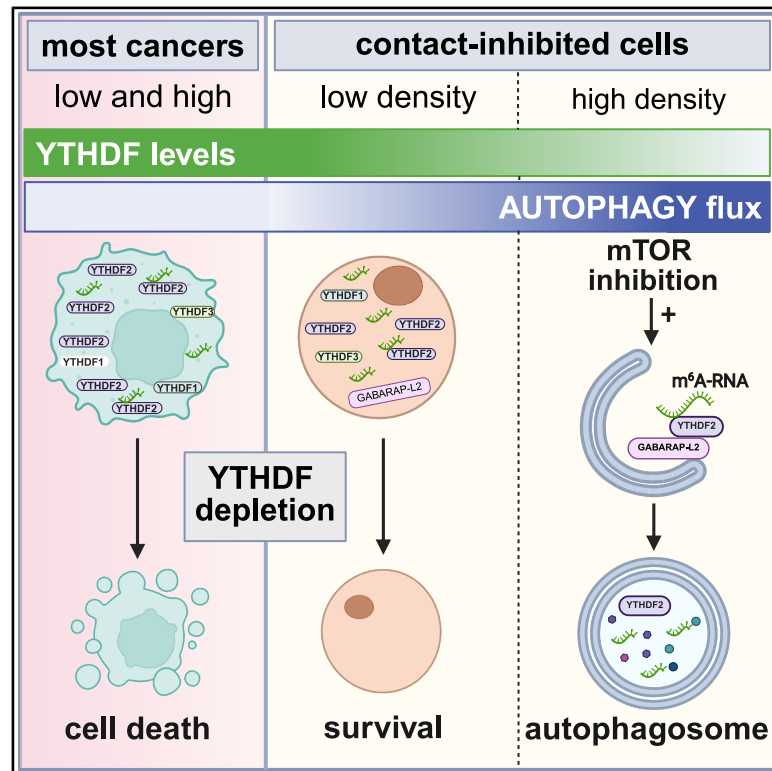


YTHDF proteins and m⁶A-RNA clients undergo autophagic turnover during contact inhibition

Graphical abstract



Authors

Hung Ho-Xuan, Astrid Bruckmann, Lautaro Natali, ..., Melina M. Musri, Gunter Meister, Alexandra Stolz

Correspondence

ho@med.uni-frankfurt.de (H.H.-X.),
gunter.meister@ur.de (G.M.),
stolz@em.uni-frankfurt.de (A.S.)

In brief

Ho-Xuan et al. show that YTHDF proteins, commonly elevated in cancers, are selectively degraded upon contact inhibition through autophagy. They identify YTHDF2 as an autophagy receptor that binds GABARAP L2 and mediates the co-degradation of m⁶A-modified RNA in cells.

Highlights

- YTHDFs are downregulated upon contact inhibition by constant autophagic turnover
- YTHDF2 selectively interacts with GABARAP L2 in cells
- YTHDF2 serves as a receptor for m⁶A-RNA co-sequestration into autophagosomes
- Depletion of YTHDF proteins induces cancer-specific cell death



Article

YTHDF proteins and m⁶A-RNA clients undergo autophagic turnover during contact inhibition

Hung Ho-Xuan,^{1,2,3,*} Astrid Bruckmann,³ Lautaro Natali,^{1,2,4} Cristian Prieto-Garcia,² Jan F.M. Stuke,⁵ Lorene Brunello,^{1,2} Alexandre Vicente,⁶ Alexander Pfab,³ Hagen Wesseling,⁶ Sara Cano-Franco,^{1,2} Anshu Khatri,⁷ Simone Larivera,³ Pablo Sanz-Martinez,^{1,2} Benjamin de la Cruz-Thea,^{3,4} Anne-Claire Jacomin,^{1,2} Jan Prochazka,⁸ Regina Feederle,^{9,10} Volker Dötsch,⁷ Radislav Sedlacek,⁸ Gerhard Hummer,^{5,11} Stefanie Kaiser,⁶ Ivan Dikic,^{1,2} Melina M. Musri,⁴ Gunter Meister,^{3,12,*} and Alexandra Stolz^{1,2,12,13,*}

¹Buchmann Institute for Molecular Life Sciences, Goethe University Frankfurt, Frankfurt am Main 60438, Germany

²Institute of Biochemistry II, Faculty of Medicine, Goethe University Frankfurt, Frankfurt am Main 60590, Germany

³Regensburg Center for Biochemistry (RCB), Laboratory for RNA Biology, University of Regensburg, 93053 Regensburg, Germany

⁴Instituto de Investigación Médica Mercedes y Martín Ferreyra, Consejo Nacional de Investigaciones Científicas y Técnicas (INIMEC-CONICET), Universidad Nacional de Córdoba, Córdoba 5016, Argentina

⁵Department of Theoretical Biophysics, Max Planck Institute of Biophysics, Frankfurt am Main 60438, Germany

⁶Institute of Pharmaceutical Chemistry, Goethe University Frankfurt, Frankfurt am Main 60438, Germany

⁷Institute of Biophysical Chemistry and Center for Biomolecular Magnetic Resonance, Goethe University Frankfurt, 60438 Frankfurt, Germany

⁸Czech Centre for Phenogenomics, Institute of Molecular Genetics of the Czech Academy of Sciences, 25250 Vestec, Czechia

⁹Core Facility Monoclonal Antibodies, Helmholtz Zentrum München, German Research Center for Environmental Health GmbH, 85764 Neuherberg, Germany

¹⁰Munich Cluster for Systems Neurology (SyNergy), 81377 Munich, Germany

¹¹Institute of Biophysics, Goethe University Frankfurt, 60438 Frankfurt am Main, Germany

¹²These authors contributed equally

¹³Lead contact

*Correspondence: ho@med.uni-frankfurt.de (H.H.-X.), gunter.meister@ur.de (G.M.), stolz@em.uni-frankfurt.de (A.S.)

<https://doi.org/10.1016/j.celrep.2025.116188>

SUMMARY

The YTHDF protein family plays a critical role in cancer development by recognizing and regulating the stability of N⁶-methyladenosine (m⁶A)-modified RNA. Here, we reveal an autophagy-dependent mechanism controlling YTHDF protein levels. Using contact inhibition as a cellular model system, we show YTHDF proteins to be rapidly degraded, coinciding with increased autophagy and decreased mTOR activity. Upon pharmacological mTOR inhibition, YTHDF2 is also downregulated via lysosomal degradation. YTHDF2 selectively interacts with the autophagy modifier GABARAP L2 through LC3-interacting region (LIR) motifs in its unstructured N- and C-terminal regions. Autophagic YTHDF2 downregulation results in the co-degradation of its bound m⁶A-modified RNA clients. While YTHDF depletion induces cell death in contact-inhibition-deficient HCT116 cancer cells, contact-inhibited MRC5 and RPE1 cells remain unaffected. Our findings uncover a regulatory pathway that governs YTHDF protein stability with significant implications for cancer biology and cell fate determination and suggest the existence of an autophagy-mediated degradation pathway for m⁶A-modified RNA.

INTRODUCTION

Autophagy is a fundamental quality control and stress response pathway that mediates the degradation of cellular components via the lysosome. In selective autophagy, specific cargo is either directly engulfed by the lysosome or targeted by autophagy receptors, which facilitate sequestration into autophagosomes (macroautophagy; hereafter referred to as autophagy).^{1,2} The membrane of forming autophagosomes is decorated with lipidated members of the LC3/GABARAP family, which interact with proteins containing LC3-interacting regions (LIRs), including autophagy receptors that tether cargo to the autophagic machinery.³ A highly dynamic and complex molecular system coordinates the selective lysosomal degradation of diverse cargo, which is subject to regulation by phosphorylation cascades

orchestrated by the mTOR complex. In recent years, an interplay between autophagy and RNA with an impact on the intracellular transport and decay of selected RNAs has emerged.⁴

Among RNA modifications, N⁶-methyladenosine (m⁶A) is the most abundant internal modification in eukaryotic mRNAs.⁵ m⁶A dynamically regulates RNA metabolism—including splicing, nuclear export, localization, translation, and degradation—through its recognition by specific reader proteins.⁶ These modifications are deposited by the METTL3/METTL14 methyltransferase complex at consensus DRACH motifs (D=A, G or U; R=G or A; H=A, C or U)^{7–10} and then interpreted by the diverse set of m⁶A readers. Reader, writer, and eraser protein networks thus tightly coordinate m⁶A landscapes during processes such as development, differentiation, and proliferation.⁵ Dysregulation of this axis is implicated in numerous diseases, including cancer.^{11,12}



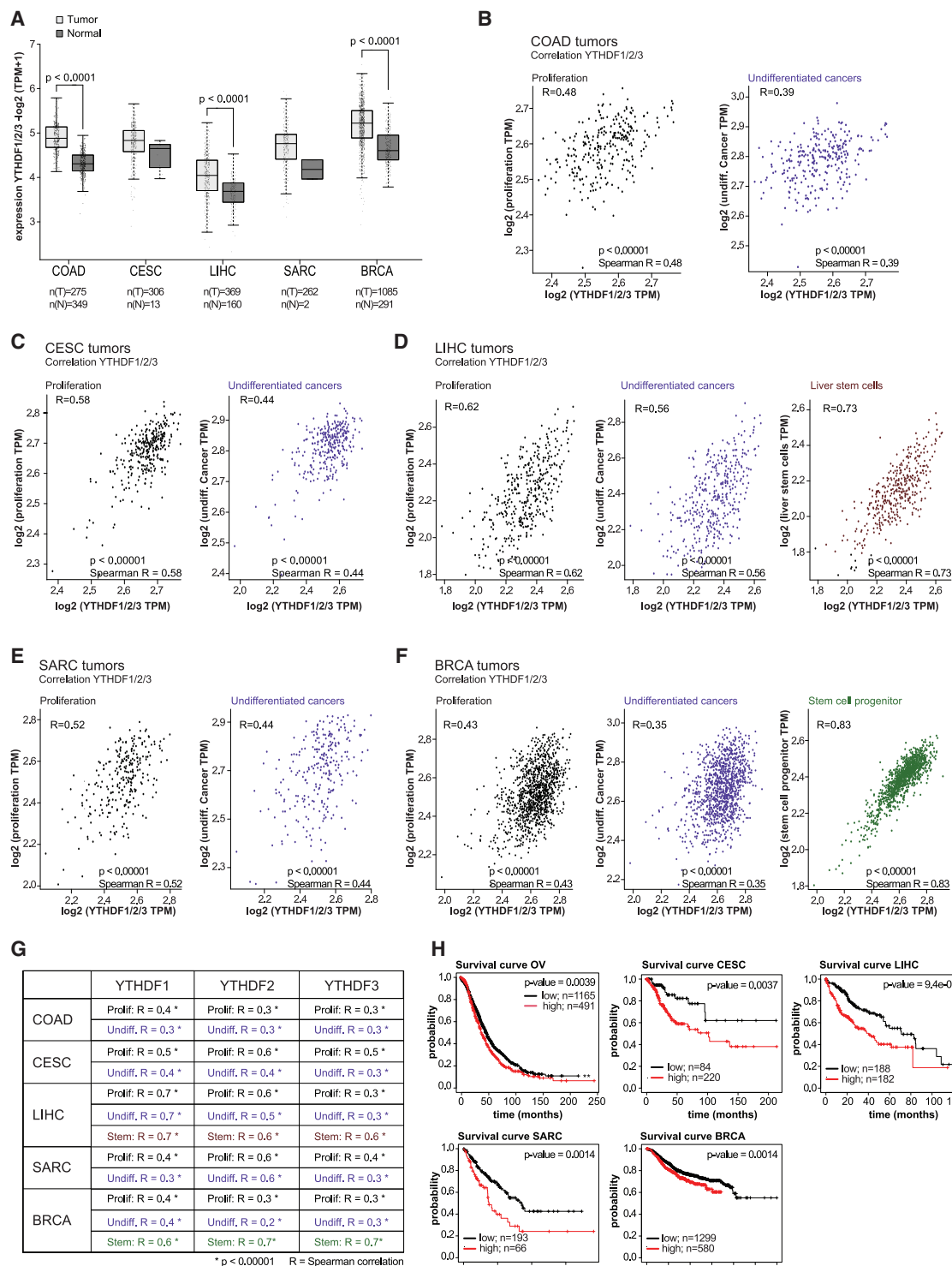


Figure 1. RNA levels of YTHDF proteins are upregulated in aggressive tumors

(A) mRNA expression of YTHDF1, YTHDF2, and YTHDF3 genes (YTHDF1/2/3) in tumor and normal non-transformed tissue for different cancer entities, including colon adenocarcinoma (COAD; tumor $n = 275$; normal $n = 349$), cervical squamous cell carcinoma and endocervical adenocarcinoma (CESC; tumor $n = 306$; normal $n = 13$), liver hepatocellular carcinoma (LIHC; tumor $n = 369$; normal $n = 160$), sarcoma (SARC; tumor $n = 262$; normal $n = 2$), and breast invasive carcinoma (BRCA; tumor $n = 1,085$; normal $n = 291$). Gene expression presented as $\log_2(\text{TPM}+1)$, where TPM is transcripts per million. Gepia2 software has been described previously.²⁷

(legend continued on next page)

Several RNA-binding proteins, including hnRNPs, FMRP, and IGF2BP1–3, recognize m⁶A-modified transcripts.^{13–16} However, the best-characterized m⁶A readers are the YTH domain-containing proteins. In humans, five such proteins exist: YTHDF1–3, which form a protein family, and the more divergent YTHDC1 and YTHDC2.¹⁷ Crosslinking-immunoprecipitation (CLIP) studies have demonstrated overlapping m⁶A binding sites among YTH proteins, suggesting functional redundancy.^{9,16–20} YTHDC1 primarily binds nuclear transcripts, while YTHDF1–3 bind cytoplasmic m⁶A sites, where they regulate mRNA stability and translation.^{17,21}

Given their roles in mRNA regulation and developmental processes, YTH proteins are increasingly recognized as critical regulators in cancer.¹² Aberrant expression of YTH proteins has been observed in multiple cancer types. Recent work revealed that YTHDF2 promotes the turnover of cell-cycle-related mRNAs and is downregulated during cell cycle progression. Its depletion delays mitotic entry and suppresses proliferation in HeLa cells.²² Moreover, YTHDF2 is overexpressed in glioblastoma, where its stability is controlled by epidermal growth factor receptor (EGFR)/SRC/ERK-mediated phosphorylation, highlighting the importance of its post-translational regulation.²³

In this study, we report that YTHDF proteins are specifically downregulated upon contact inhibition—a key mechanism that maintains tissue homeostasis and is frequently lost in cancer.^{24,25} We demonstrate that YTHDF levels decrease in high-density (HD), contact-inhibited cells but remain stable in cell lines lacking contact inhibition. Using HCT116 cells as a model of deficient contact inhibition, we show that YTHDF proteins function redundantly in regulating cell proliferation, cell cycle progression, and apoptosis. Furthermore, we identify autophagy as a key pathway in the degradation of YTHDF proteins under contact-inhibited conditions, with mTOR signaling influencing this process even at low cell density. Notably, we find that in cells, YTHDF2 directly binds GABARAP L2, linking it to the autophagic machinery. Autophagosome isolation reveals that m⁶A-modified RNA is co-degraded with YTHDF2, suggesting an alternative mechanism of RNA turnover. Together, our findings identify YTHDF2 as an autophagy-associated m⁶A reader and uncover an autophagy pathway targeting m⁶A-modified RNA, with significant implications for cell fate and cancer biology.

RESULTS

YTHDF expression correlates with cancer proliferation and differentiation status

YTHDF family members, particularly YTHDF2, have previously been linked to cancer development.¹² To better understand their role and therapeutic potential, we analyzed public transcriptomic

and proteomic datasets. All three YTHDF family members were consistently upregulated in multiple cancer types compared to healthy tissues (Figures 1A and S1A), and their expression correlated with high proliferation rates, low differentiation states, and advanced tumor stages (Figures 1B–1G and S1B), which is in line with previous reports.^{12,26} Notably, lower YTHDF1–3 expression was associated with improved chemotherapy responses in colorectal and ovarian cancers (Figures S1C and S1D) and higher patient survival (Figure 1H), highlighting their clinical relevance.

Proteomic analyses confirmed elevated YTHDF protein levels in tumors versus adjacent normal tissue (Figures S1E–S1G). This upregulation was specific to YTHDFs and not seen across the m⁶A methylation machinery (Figures S1H–S1J), suggesting a distinct pathological role. As an example, we further highlight expression details of individual YTHDF proteins in colorectal cancer and its adjacent normal tissue (Figures S1K–S1M).

MYC overexpression leads to an undifferentiated phenotype and induces the formation of highly proliferative, aggressive tumors.²⁸ It was previously shown that YTHDF2 is essential for supporting cell growth and viability in the context of MYC-driven processes, both at the cellular level and during tumor formation.²⁹ In MYC-driven liver tumors, YTHDF proteins were upregulated and strongly correlated with MYC expression (Figures S2A and S2B), indicating that they are likely MYC-regulated effectors critical for sustaining tumor growth and that understanding the pathways that regulate YTHDF protein expression is of specific relevance for the development of efficient treatments of MYC-driven cancers (Figures S2A–S2E).

YTHDF family members are downregulated in contact-inhibited cell lines

A common feature of cancer cells is that they are deficient in contact inhibition. Contact inhibition is a key physiological mechanism that halts cell proliferation upon reaching confluence, often accompanied by cellular differentiation. In contrast, cancer cells typically lose contact inhibition and maintain an undifferentiated, hyperproliferative state. To investigate whether YTHDF protein expression is influenced by contact inhibition, we analyzed non-cancerous human cell lines MRC5 (fetal lung fibroblasts) and RPE1 (retinal pigment epithelial cells), both of which retain contact inhibition under standard culture conditions. When examining cells cultured at low density (LD; <70% confluent) and HD (100% confluent for 48 h, see STAR Methods), we observed a significant downregulation of all three YTHDF family members when HD was reached (Figure 2A and 2B). This pattern was conserved in additional contact-inhibited cell lines, including mouse NIH-3T3 and rat NRK cells (Figures 2A and 2B), suggesting a cross-species regulatory mechanism. As expected, HD cultures showed markers of cell-cycle

(B–G) Spearman's correlation coefficient of YTHDF1/2/3 mRNA expression and consensus human gene datasets (proliferation: BENPORATH_PROLIFERATION, M2114; undifferentiated cancer: RHODES_UNDIFFERENTIATED_CANCER, M8365; liver stem cells: YAMASHITA_LIVER_CANCER_STEM_CELL_UP, M16956; and stem cell progenitor BRCA: ZHANG_BREAST_CANCER_PROGENITORS_UP, M15150) in different cancer entities, including COAD ($n = 275$), CESC ($n = 306$), LIHC ($n = 369$), SARC ($n = 262$), and BRCA ($n = 1,085$). For graphics in (B)–(F), Spearman's coefficient was calculated between a gene list comprising YTHDF genes (YTHDF1/2/3) and indicated datasets. For the table in (G), the correlation was calculated for individual expression of YTHDF1, YTHDF2, and YTHDF3 genes and indicated datasets. R, Spearman's correlation coefficient.

(H) Kaplan-Meier survival curves of patients with ovarian cancer (ovarian cancer; $n = 1656$), CESC ($n = 304$), LIHC ($n = 370$), SARC ($n = 259$), and BRCA ($n = 1,879$) stratified by high and low YTHDF1, YTHDF2, and YTHDF3 gene expression. p values were calculated using log-rank test.

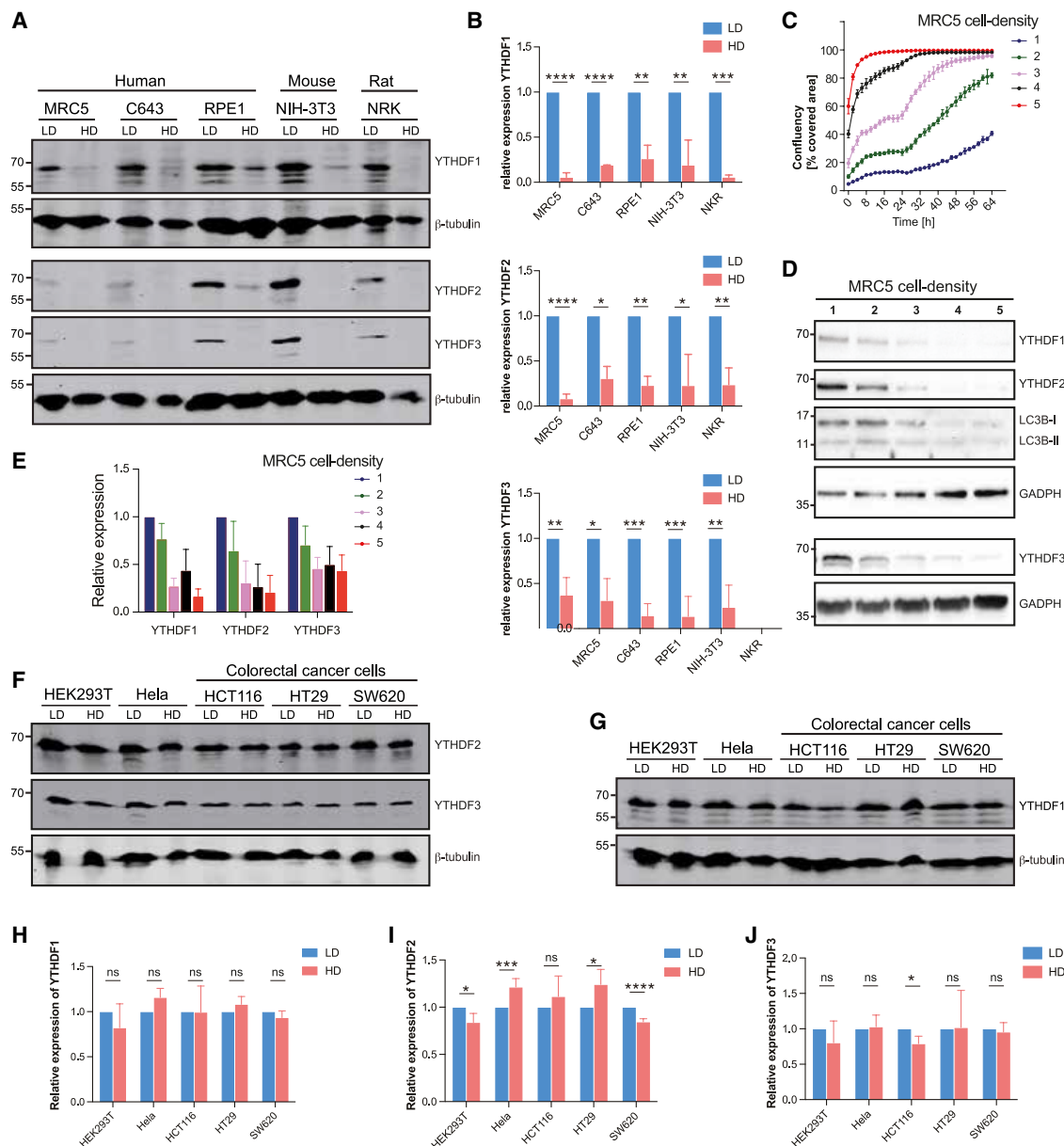


Figure 2. YTHDF protein levels are regulated by contact inhibition

(A) Representative western blot analysis of YTHDF1 protein levels at low density (LD; ~30% confluence) and high density (HD; 48 h after reaching 100% confluence) in contact-inhibited cells.

(B) Quantification of (A) and related western blots. Error bars represent the standard deviation (SD) from at least two biological replicates. Statistical analyses were calculated using Student's t test by GraphPad Prism 10. * p < 0.05, ** p < 0.01, *** p < 0.001, and **** p < 0.0001.

(C) MRC5 cells were seeded at different densities, and cell growth was measured every 2 h for 64 h using the Incucyte S3. Error bars represent SD. n = 3.

(D) After 64 h of growth, MRC5 cells were harvested for western blot analysis with indicated antibodies.

(E) Quantification YTHDF1–3 expression levels of (D) and related western blots. Error bars represent SD from three biological replicates.

(F and G) Western blot of non-contact-inhibited human cell lines, including HEK293T, HeLa, and the colorectal cancer cell lines HCT116, HT29, and Sw620.

(H–J) Quantification of the expression of YTHDF1 (I), YTHDF2 (J), and YTHDF3 (K) of (F) and (G) and related western blots. Error bars correspond to SD; n \geq 3. Statistics analysis was calculated using Student's t test by GraphPad Prism 10. * p < 0.05, ** p < 0.01, *** p < 0.001, **** p < 0.0001, and ns, not significant.

arrest: increased p27 and decreased CDK6 expression (Figure S2F), along with G1-phase accumulation confirmed by fluorescence-activated cell sorting (FACS) analysis (Figure S2G). Since we observed a drastic decrease in YTHDF protein

expression in cells grown at HD compared to LD, we aimed to investigate the dynamics of YTHDF protein expression. To this end, we cultured MRC5 cells at five different densities (Figure 2C) and performed western blot analysis after 64 h

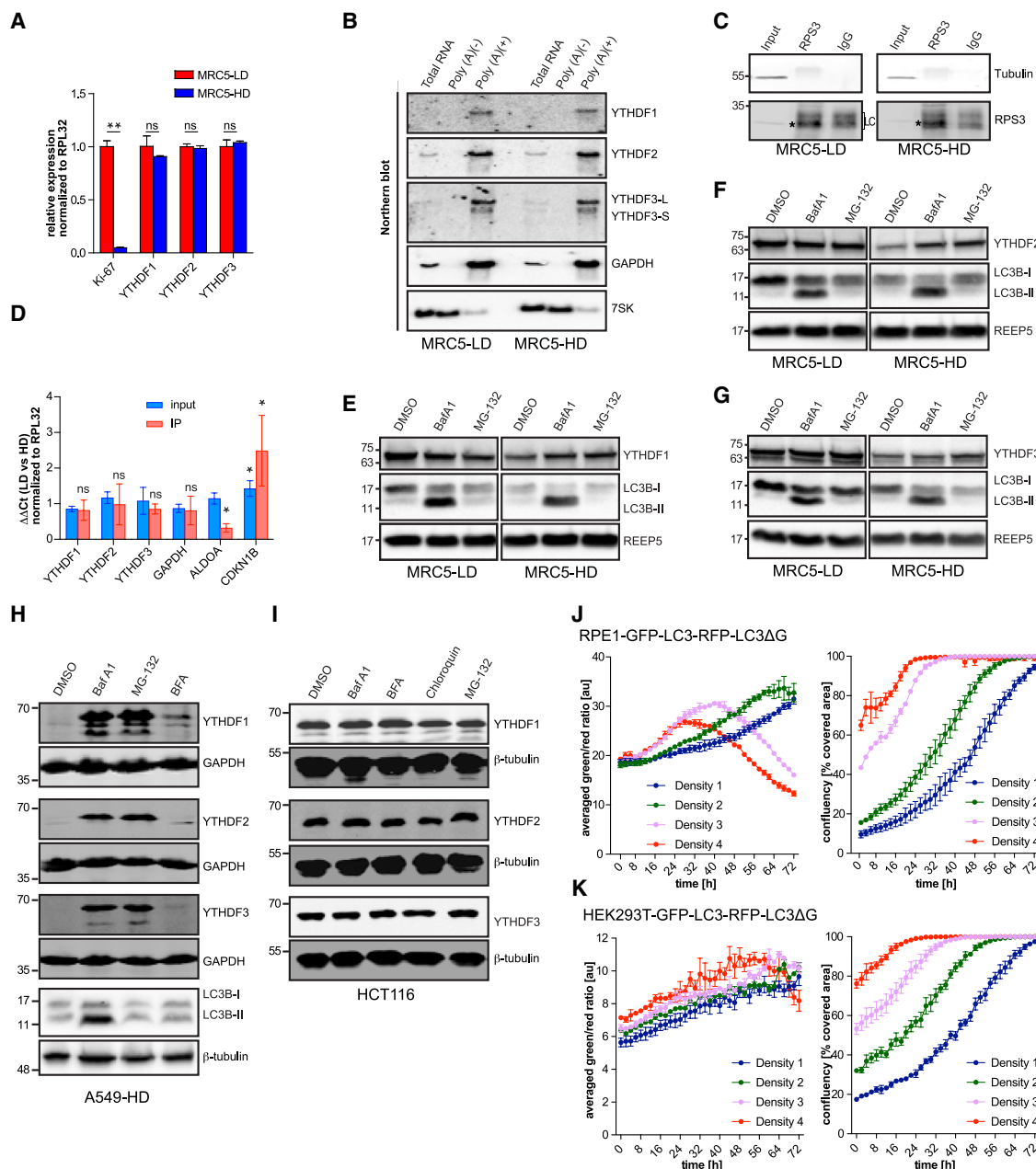


Figure 3. YTHDF expression is regulated on the protein level

(A) Relative expression of YTHDF mRNA levels quantified by qPCR and normalized to RPL32 in MRC5 cells under LD and HD culturing conditions. Ki67: proliferation marker. Data represent mean with standard deviation (SD). Statistics analysis was calculated using Student's t test by GraphPad Prism 10. ** $p < 0.01$ and ns, not significant.

(B) Northern blot analysis of YTHDF transcripts in MRC5 cells under LD and HD culturing conditions after fractionation of poly(A)⁺ RNA and poly(A)⁻ RNA. GAPDH: positive control of poly(A)⁺ RNA; 7SK: positive control of poly(A)⁻ RNA.

(C) Ribosomal protein RPS3 purified from MRC5 cells cultured at LD and HD. LC, light-chain background; *, RPS3-specific signal.

(D) Ribo-IP-qPCR of total YTHDF1–3 mRNA (input), as well as actively translated YTHDF1–3 mRNA (IP), purified from LD and contact-inhibited (HD) MRC5 cells. ALDOA and CDKN1B served as controls. $\Delta\Delta\text{CT}$ values were normalized to RPL32 (HD versus LD). Error bars correspond to SD; $n \geq 3$. Significance was analyzed by Student's t test. * $p < 0.05$.

(E–G) Western blot analysis of MRC5 cells under LD and HD culturing conditions treated with 300 nM bafilomycin A1 (BafA1), 10 μM MG-132, or 0.1% DMSO for 4 h. REEP5: loading control.

(H) Western blot analysis of YTHDF1–3 and LC3 in A549 cells under HD culturing conditions treated with 300 nM BafA1, 10 μM MG-132, BFA (brefeldin A), or 0.1% DMSO for 4 h. GAPDH and beta-tubulin: loading controls.

(legend continued on next page)

(Figures 2D and 2E), indicating a gradual decrease in YTHDF protein expression with increasing cell density. Taken together, these results demonstrate that YTHDF protein expression is consistently downregulated upon the onset of contact inhibition in non-transformed mammalian cells.

YTHDF protein levels remain high in cells lacking contact inhibition

Loss of contact inhibition is a hallmark of cancer, enabling uncontrolled proliferation despite high cell density.²⁵ This can also be observed in most cancer-derived cell lines, which continue dividing beyond confluence. To investigate whether the density-dependent downregulation of YTHDF proteins is specific to contact-inhibited cells, we examined YTHDF1–3 expression in several cancer cell lines that lack contact inhibition, including HeLa (human cervix carcinoma), HCT116 (human colorectal carcinoma), HT29 (human colorectal adenocarcinoma), and SW620 cells (Dukes' type C colorectal adenocarcinoma). Across all tested cell lines, YTHDF protein levels remained unchanged between LD and HD conditions (Figures 2F–2J and S2H), indicating a loss of density-responsive regulation.

To ensure that the misregulation of YTHDF protein levels is indeed connected to the loss of contact inhibition and not a general phenomenon of all cancer cell lines, we also analyzed two control lines: a cancer cell line with stemness properties (C643, human anaplastic thyroid carcinoma cell line; Figure 2A) and a non-cancerous cell line, which lost contact inhibition (HEK293T: human embryonic kidney cell line; Figures 2F and 2G). As expected, YTHDF levels were downregulated at HD in C643 cells but remained stable in HEK293T cells. This is consistent with our hypothesis that the regulation of YTHDF protein levels at HD is connected to contact inhibition and potentially the differentiation status of a cell.

YTHDF protein levels are regulated via autophagy

To define the mechanism underlying YTHDF downregulation during contact inhibition, we first assessed mRNA levels in contact-inhibited MRC5 cells. qPCR and Northern blot analyses revealed that YTHDF1–3 transcripts remained stable between LD and HD cultures, while the proliferation marker *Ki67* was significantly reduced (Figure 3A and 3B). We next sought to determine whether its mRNA translation was affected by contact inhibition. Ribosome immunoprecipitation followed by RT-qPCR showed no changes in YTHDF mRNA association with ribosomes at HD, while controls (*ALDOA* and *CDKN1B*) exhibited expected shifts (Figures 3C and 3D). This corresponded to the upregulation of p27 and the downregulation of *ALDOA* protein levels, consistent with previous reports.^{30,31} These results suggest that YTHDF expression is not regulated at either the transcriptional or translational level.

To test the regulation of YTHDF at the protein level, MRC5 cells were grown at LD and HD and treated for 4 h with MG-132 (proteasome inhibitor) or bafilomycin A1 (BafA1; autophagy

inhibitor) before lysates were analyzed by western blotting against endogenous YTHDF proteins (Figures 3E–3G). Inhibition of proteasomal or autophagic pathways led to significant accumulation of YTHDF proteins in HD-cultured MRC5 and A549 cells (Figures 3E–3H)²² but not in contact-inhibition-deficient HCT116 cells (Figure 3I). These findings indicate that YTHDF downregulation upon contact inhibition is mediated through coordinated degradation by both the ubiquitin-proteasome system (UPS) and autophagy.

Autophagy is activated upon contact inhibition

While proteasomal degradation of the YTHDF2 protein has been previously reported,²² its autophagic turnover remains unexplored. To determine whether autophagy is activated upon the onset of contact inhibition, we used a series of LC3-based autophagy reporter cell lines stably expressing the reporter GFP-LC3-RFP-LC3ΔG, which enables quantitative autophagy flux measurements independent of the cell number.³² Cells were analyzed using live-cell imaging in a 384-well format, and in this setting, a decrease in ratio reflects an activation of autophagy (low ratio = high flux).³³ Live-cell imaging revealed robust autophagy activation in contact-inhibited RPE1, MRC5, BJ, and U2OS cells at high confluence (Figures 3J and S3–S5). In contrast, HEK293T cells, which lack contact inhibition, showed no change in autophagy flux upon reaching confluence (Figure 3K). These findings suggest that autophagy is specifically induced as part of the contact inhibition response and that it contributes to the observed YTHDF protein degradation.

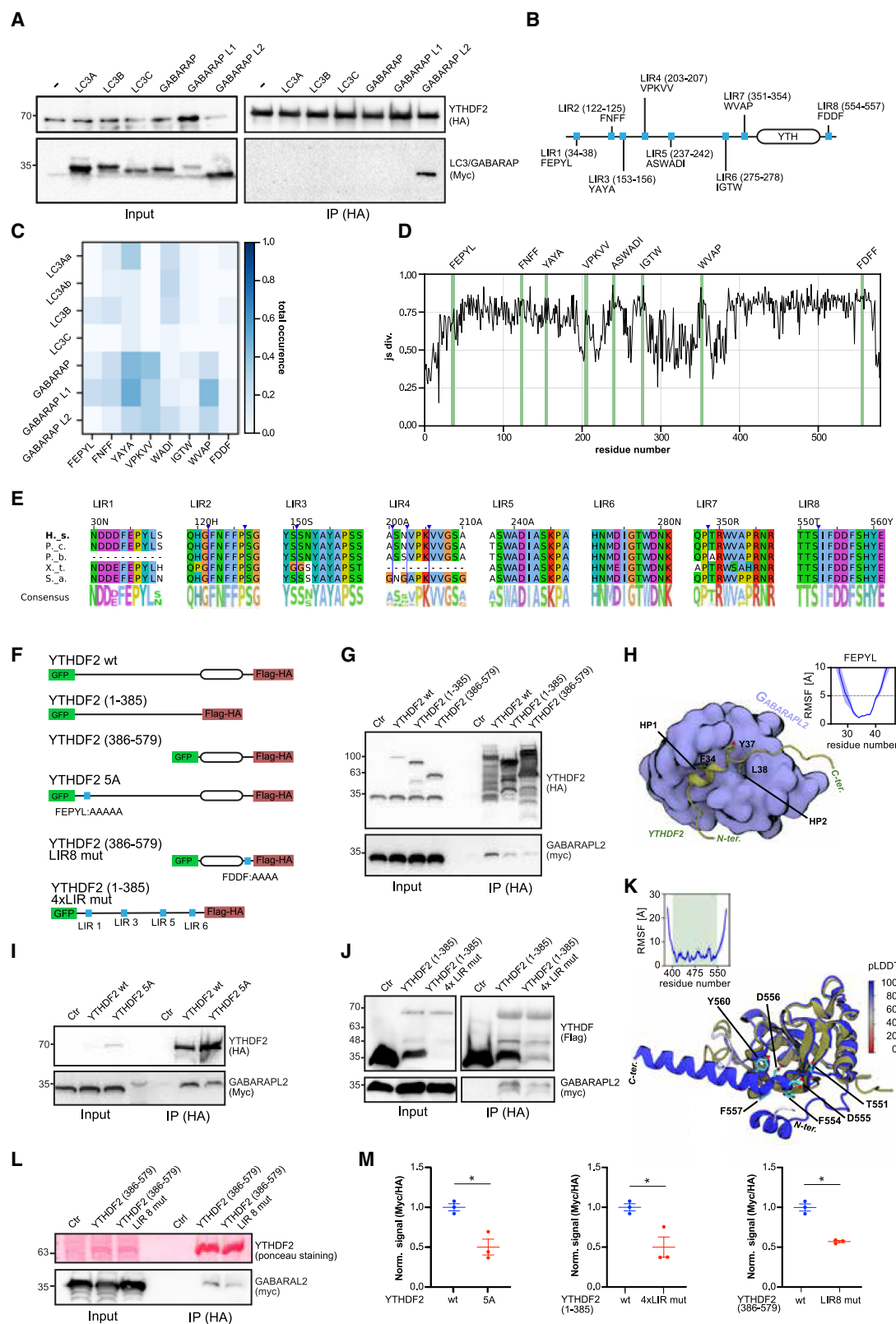
YTHDF2 interacts with the autophagy machinery via its LIR motifs

We next investigated how YTHDF2 is targeted for autophagic degradation. Glutathione S-transferase (GST) pull-down assays using GST-tagged LC3/GABARAP proteins and lysates from cells overexpressing FLAG-hemagglutinin (HA)-tagged YTHDF2 (FH-YTHDF2) revealed binding to all six LC3/GABARAP family proteins, with a preference for GABARAP subfamily members *in vitro* (Figure S6A). Co-immunoprecipitation (coIP) assays using anti-HA beads in cells co-expressing FH-YTHDF2 and Myc-tagged LC3/GABARAPs revealed preferred interactions between YTHDF2 and GABARAP L2 *in cellulo* (Figure 4A). Of note, initial pull-down experiments using anti-FLAG beads for YTHDF2 pull-down resulted in a dominant, false-positive enrichment of LC3C. Due to sequence similarity between the FLAG tag and LC3C, the FLAG beads directly precipitate LC3C (Figure S6B) and thereby mimic an approximate 1:1 interaction ratio between YTHDF2 and LC3C.

We subsequently combined AlphaFold predictions with molecular dynamics (MD) simulations to identify LIR motifs in YTHDF2, primarily located within the unstructured regions of YTHDF2. An *in silico* peptide screen with AlphaFold2 Multimer identified eight putative LIR motifs with medium to high confidence scores that may facilitate the interaction with GABARAP

(I) Western blot analysis of YTHDF1–3 in HCT116 cells treated with 300 nM BafA1, 10 μM MG-132, 10 μM chloroquine, 10 μg/mL BFA, or 0.1% DMSO for 4 h. Beta-tubulin: loading control.

(J and K) Autophagy flux (low ratio = high flux) and confluency of RPE1 (J) and HEK293T (K) cells stably expressing the autophagy flux reporter EGFP-LC3-RFP-LC3ΔG and seeded at four different densities.



(legend on next page)

L2 (Figures 4B and 4C). These LIRs are highly conserved across species (Figures 4D and 4E). Interestingly, two additional motifs (data not shown) were predicted within the structured YTH domain,³⁴ although their likely inaccessibility suggests that they may rather participate in quality control under aberrant folding conditions.

To test functional binding, we generated FLAG/HA-tagged N-terminal (amino acids [aa] 1–385) and C-terminal (aa 386–579) fragments of YTHDF2. Both fragments interacted with GABARAP L2 in co-immunoprecipitation assays (Figure S6C), although the N-terminal fragment displayed instability in cells. To stabilize it, we engineered constructs with an N-terminal EGFP tag and a C-terminal FLAG/HA tag. This approach maintained the fragment expression and preserved binding to GABARAP L2 (Figures 4F and 4G).

Performing an AlphaFold3 prediction with full-length YTHDF2 and GABARAP L2, the residues 34-FEPYL-37 (LIR1) and 275-IGTW-278 (LIR6) showed interactions with GABARAP L2 in different models (Figures S6D and S6E). MD simulations of a 24-residue YTHDF2 fragment containing the candidate LIR1 in complex with GABARAP L2 further supported the stability of the predicted interaction with residue F34 inserted into hydrophobic pocket 1 (HP1) of GABARAP L2, while L38 interacts with HP2 (Figure 4H). To validate specific LIR motifs, we mutated selected key residues. Mutation of LIR1's five core residues to alanine (YTHDF2-5A) significantly impaired binding to GABARAP L2 (Figures 4F–4I and 4M, left). Additional muta-

genesis of LIR3, -5, and -6 in the N-terminal region (4xLIR mutant) reduced binding to a similar extent as the 5A mutant, indicating that LIR1 is the primary LIR (Figures 4F–4J and 4M, middle). We then tested the contribution of the C-terminal LIR8, located adjacent to the YTH domain in a region AlphaFold3 predicted to be folded but MD simulations revealed to be structurally dynamic (Figure 4K). Mutation of this motif significantly reduced binding to GABARAP L2 (Figures 4F, 4L, and 4M, right), consistent with its predicted accessibility and role in direct interaction. Together, these data establish that YTHDF2 directly engages the autophagy machinery via multiple conserved LIR motifs, with a prominent role for LIR1 and LIR8.

YTHDF levels are controlled by mTOR signaling

Given the connection between autophagy and mTOR signaling, we next examined whether mTOR activity regulates YTHDF2 degradation. We observed a reduction in S6K phosphorylation—a downstream marker of mTOR activity—at high cell density (Figure 5A), consistent with autophagy induction during contact inhibition and a previous report.³⁵ Analysis of public proteomic datasets³⁶ revealed decreased YTHDF2 and YTHDF3 protein levels in Torin1-treated cells (Figures 5B, S6F, and S6G), which we confirmed in MRC5 and HEK293T cells (Figures 5C and 5D).

This not only suggests that altered mTOR and autophagy activity is part of active contact inhibition but also that we may use

Figure 4. Bioinformatic predictions and validation of potential (non-)canonical LIRs

- (A) Co-immunoprecipitation analysis in transiently transfected HEK293T cells co-expressing Myc-tagged LC3/GABARAP proteins and FLAG-HA-tagged YTHDF2 using anti-HA beads.
- (B) Schematic overview of 8 different predicted LIRs in YTHDF2 protein.
- (C) Summarized results from a systematic *in silico* peptide screen using AlphaFold2.3. We screened 16-, 36-, and 52-residue fragments (75% overlap) of YTHDF2 (wild-type [WT] sequence and phosphomimetic sequence) against all human ATG8s. Shown is the fraction of the fragments for which an interaction with the respective ATG8 is predicted that uses (parts of) the respective shown motif (“total occurrence”). Shown are only the most promising (reliably predicted and not buried in the folded domain) candidate LIRs, which we used for experimental validation.
- (D) Sequence conservation quantified by Jensen-Shannon divergence (higher values correspond to higher conservation) for a multiple sequence alignment of 567 vertebrate YTHDF2 orthologs. Residue numbers correspond to the human sequence, and insertions are hidden. Sequence positions of candidate LIRs are indicated as green bars.
- (E) Conservation and consensus motif of 8 predicted LIRs using software Jalview (<https://www.jalview.org/>) and WebLogo (<https://weblogo.berkeley.edu/>).
- (F) Schematic overview of different YTHDF2 constructs expressing: YTHDF2 WT, the N-terminal part of YTHDF2 (1–385), the C-terminal part of YTHDF2 (386–579), a full-length 5 alanine mutant of the FEPYL LIR candidate YTHDF2 (5A), the C-terminal part of YTHDF2 containing a 4 alanine mutant of the LIR candidate 8 (LIR8 mut), and the N-terminal part of YTHDF2 with mutations in LIR candidates 1, 3, 5, and 6 (4xLIR mut). All constructs are double tagged (N terminus with GFP and C terminus with FLAG/HA).
- (G) Co-immunoprecipitation analysis in transiently transfected HEK293T cells co-expressing Myc-tagged GABARAP L2 and FLAG-HA plasmid control, YTHDF2, and N-terminal or C-terminal fragments of YTHDF2 using anti-HA beads.
- (H) Final structure of a 24-residue YTHDF2 fragment (green cartoon) containing the candidate LIR 34-FEPYL-38 in complex with GABARAP L2 (blue surface representation with HP1 and HP2 indicated) after 1 μ s of MD simulation. The inset shows C α root-mean-square fluctuation (RMSF) values from triplicate MD simulations for the candidate LIR peptide with the trajectory being aligned on GABARAP L2. The blue-shaded area indicates the standard error of the mean.
- (I) Co-immunoprecipitation analysis in transiently transfected HEK293T cells co-expressing Myc-tagged GABARAP L2 proteins and FLAG-HA-YTHDF2 WT or LIR mutant (5A) using anti-HA beads.
- (J) Co-immunoprecipitation analysis in transiently transfected HEK293T cells co-expressing Myc-tagged GABARAP L2 and FLAG-HA-tagged GFP, YTHDF2 N-terminal (1–385) WT, or 4-LIR mutant (4xLIR mut) using anti-HA beads.
- (K) Top: average RMSF of YTHDF2 residues 383–579 (corresponds to the shown part of the AlphaFold3 model on the bottom from triplicate MD simulations). The blue-shaded area indicates the standard error of the mean and the green area the residues resolved in the crystal structure. Bottom: cartoon representation of a YTHDF2 crystal structure (RCSB PDB: 4RDN) in green and an AlphaFold3 model of full-length YTHDF2 (N-terminal intrinsically disordered region omitted for visual clarity) colored by the predicted local distance difference test (pLDDT) score. Residues of candidate LIR 554-FDDF-557 and two nearby phosphosites are highlighted in cyan.
- (L) Co-immunoprecipitation analysis in transiently transfected HEK293T cells co-expressing Myc-tagged GABARAP L2 and FLAG-HA plasmid control, YTHDF2 C-terminal (386–579) WT, or LIR8 mutant using anti-HA beads.
- (M) Quantifications of the interactions shown in (G), (I), and (J). Data represent mean with standard deviation (SD). Statistics analysis was calculated using Student's *t* test by GraphPad Prism 10. **p* < 0.05.

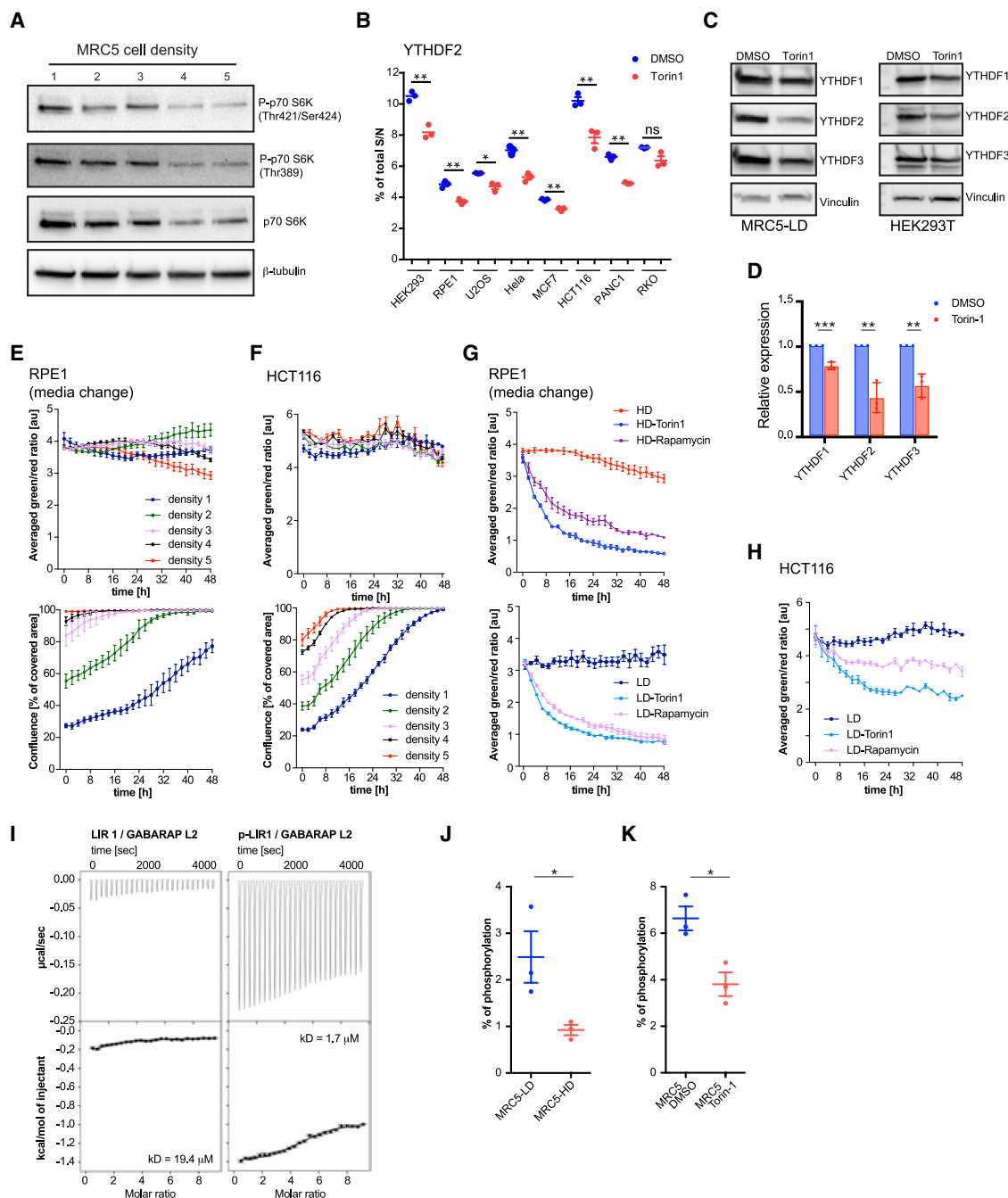


Figure 5. YTHDF proteins are regulated by mTOR signaling

(A) MRC5 cells were seeded at increasing densities and harvested after 64 h of growth for western blot (WB) analysis with indicated antibodies against the markers of mTOR signaling pathway.

(B) Relative protein expression level of S39 phosphorylation on YTHDF2 proteins in different cell lines upon treatment with 150 nM Torin1. Data were extracted and reanalyzed from a dataset published previously.³⁶ Statistics analysis was calculated using Student's t test by GraphPad Prism 10. * $p < 0.05$, ** $p < 0.01$, and ns, not significant.

(C) Representative WB analysis of MRC5 and HEK293T cells cultured at LD and treated with 250 nM Torin1/0.1% DMSO.

(D) Quantification of the expression of YTHDF1–3 in MRC5 cells cultured at LD upon treatment with Torin-1. Data represent mean with standard deviation (SD). Statistics analysis was calculated using Student's t test (** $p < 0.01$ and *** $p < 0.001$) by GraphPad Prism 10.

(E and F) A single clone of RPE1 (E)- and a single clone of HCT116 (F) inducibly expressing EGFP-YTHDF2-p2A-mCherry were seeded at 5 different densities, and the turnover of YTHDF2 (top) and cell growth (bottom) were measured over time by live-cell imaging.

(legend continued on next page)

mTOR inhibitors to mimic the state of contact inhibition with respect to YTHDF downregulation. We generated stable, doxycycline-inducible cell lines with the construct EGFP-YTHDF2-p2A-mCherry in RPE1 (contact-inhibited) and HCT116 (non-contact-inhibited) cells. EGFP-YTHDF2 and mCherry are expressed from the same construct, where they are flanked by the self-cleaving peptide p2A, which allows the monitoring of relative YTHDF2 levels per cell, independent of the cell number, and by the ratio of green/red fluorescence. EGFP-YTHDF2 exhibits the anticipated cytoplasmic expression, and the internal control mCherry was distributed uniformly across the cells (Figure S6H). Expression was induced for 24 h before cells were seeded at five different densities. While YTHDF2 levels declined with cell density in RPE1 cells, they remained unchanged in HCT116 cells, consistent with their deficiency in contact inhibition (Figures 5E and 5F). Pharmacological mTOR inhibition using Torin1 or rapamycin caused rapid downregulation of YTHDF2 in both RPE1 cells (Figures 5G–5I) and HCT116 cells (Figure 5H), even at LD. This suggests that YTHDF proteins, their autophagic degradation, and subsequent loss of function are downstream of mTOR signaling and that cells with deficient contact inhibition have altered signaling processes upstream of mTOR.

Phosphorylation at serin 39 modulates YTHDF2 stability and autophagic targeting

Phosphorylation adjacent to LIR motifs is a known mechanism to regulate ATG8 binding and cargo selectivity during autophagy, often downstream of mTOR signaling.^{3,37} Given our identification of LIR1 as an active site mediating YTHDF2 binding to GABARAP L2 (Figure 4M), we explored the functional role of phosphorylation at serine 39 (S39), a residue immediately C-terminal to LIR1 (Figure 4E). Previous work implicated S39 phosphorylation, mediated by EGFR/SRC/ERK signaling, in stabilizing YTHDF2 in glioblastoma.²³ We performed isothermal titration calorimetry (ITC) using synthetic peptides corresponding to unmodified and phosphorylated LIR1 (p-LIR1) and assessed binding affinity to LC3B, LC3C, and GABARAP L2 (Figures 5I, S7A, and S7B). Unmodified LIR1 exhibited negligible binding to LC3C and weak binding to LC3B but bound GABARAP L2 with a dissociation constant (K_D) of 19.4 μ M, a value consistent with established LIR-ATG8 interactions. Phosphorylation at S39 significantly increased binding affinity across all tested ATG8 proteins, most notably a \sim 10-fold increase for GABARAP L2 (Figure 5I, right), aligning with the strong *in vivo* preference observed in colP experiments.

To determine whether S39 phosphorylation levels are indeed regulated during contact inhibition, we immunoprecipitated endogenous YTHDF2 from cells using a newly developed mono-

clonal antibody (clone 9G11) (Figure S7C) and performed targeted mass spectrometry via selected reaction monitoring (SRM). S39 phosphorylation levels were higher at LD and significantly reduced in HD cultures (Figures 5J and S7D). Moreover, pharmacological inhibition of mTOR with Torin1 similarly reduced S39 phosphorylation in LD conditions, mimicking the HD phenotype (Figures 5K and S7E). Reanalysis of public phosphoproteomic datasets³⁶ further supported this finding, showing decreased S39 phosphorylation following Torin1 treatment across multiple cell lines (Figure S7F).

Taken together, our data identify S39 as a phosphorylation site that contributes to YTHDF2 downregulation upon contact inhibition and imply that mTOR is a central regulator of this post-translational modification. Phosphorylation at S39 facilitates YTHDF2 engagement with the autophagy machinery, thereby linking growth control pathways to autophagic YTHDF2 degradation.

YTHDF2 facilitates autophagic degradation of m⁶A-modified RNA

While our data support a contact-inhibition- and mTOR-dependent pathway for YTHDF protein degradation via autophagy, the functional rationale for engaging both autophagy and the UPS remained unclear. Given that YTHDF proteins can be degraded by the UPS (Figures 3E–3G), we hypothesized that their selective autophagic turnover may serve a distinct biological role. Specifically, we considered whether YTHDF2-mediated autophagy specifically enables the coordinated degradation of YTHDF2-m⁶A-RNA complexes. To test this, we adapted a previously described protocol and established a FACS-based approach using a pan-GABARAP antibody (recognizing all three GABARAP proteins) to isolate autophagosomes (Figures 6A and S8A–S8D).³⁸ We utilized our inducible RPE1 stable cell line expressing EGFP-YTHDF2 and isolated autophagosomes after 4 h of Bafilomycin A1 treatment to accumulate autophagosomes. Cells were cultured under LD, HD, or LD plus Torin1 treatment. FACS analysis confirmed the presence of EGFP-YTHDF2 in autophagosomes under all conditions (Figures 6B–6D and S8E). EGFP-positive autophagosomes were more prevalent in HD cultures compared to LD, consistent with increased YTHDF2 turnover under contact inhibition (Figure 6E).

To determine whether RNA cargo is co-degraded with YTHDF2, we extracted total RNA from sorted autophagosomes. Bioanalyzer analysis revealed distinct RNA profiles in autophagosomes versus whole-cell lysates, indicating selective RNA enrichment rather than passive engulfment (Figure 6F). Normalizing RNA yields to autophagosome number, we found that EGFP-positive autophagosomes consistently contained higher RNA levels than their EGFP-negative counterparts

(G) RPE1 cells inducibly expressing EGFP-YTHDF2-p2A-mCherry were seeded at LD (bottom) and HD (top), and the turnover of YTHDF2 upon 250 nM Torin1, 250 nM rapamycin, and 0.1% DMSO treatment was measured over time by live-cell imaging.

(H) HCT116 cells inducibly expressing EGFP-YTHDF2-p2A-mCherry were seeded at LD, and the turnover of YTHDF2 upon 250 nM Torin1, 250 nM rapamycin, and 0.1% DMSO treatment was measured over time by live-cell imaging.

(I) Interaction profile of LIR1 titrated to GABARAP L2. Every measurement was done at 25°C by titrating 1,000 μ M of peptide to 20 μ M of ATG8. The top image of each figure shows the raw titration profile, and the bottom image displays the integrated heat of each titration event. The best fit of a single-site binding model is shown as a solid black line, generated by GUSI software. The resulting equilibrium dissociation constant (K_D) is mentioned at the bottom of every plot.

(J) Relative quantification of phosphorylated S39 in MRC5 cells at LD and HD.

(K) Relative quantification of phosphorylated S39 in MRC5 cells seeded at LD treated with 0.1% DMSO or 250 nM Torin-1. Data represent mean with SD. Statistics analysis was calculated using Student's t test ($p < 0.05$) by GraphPad Prism 10.

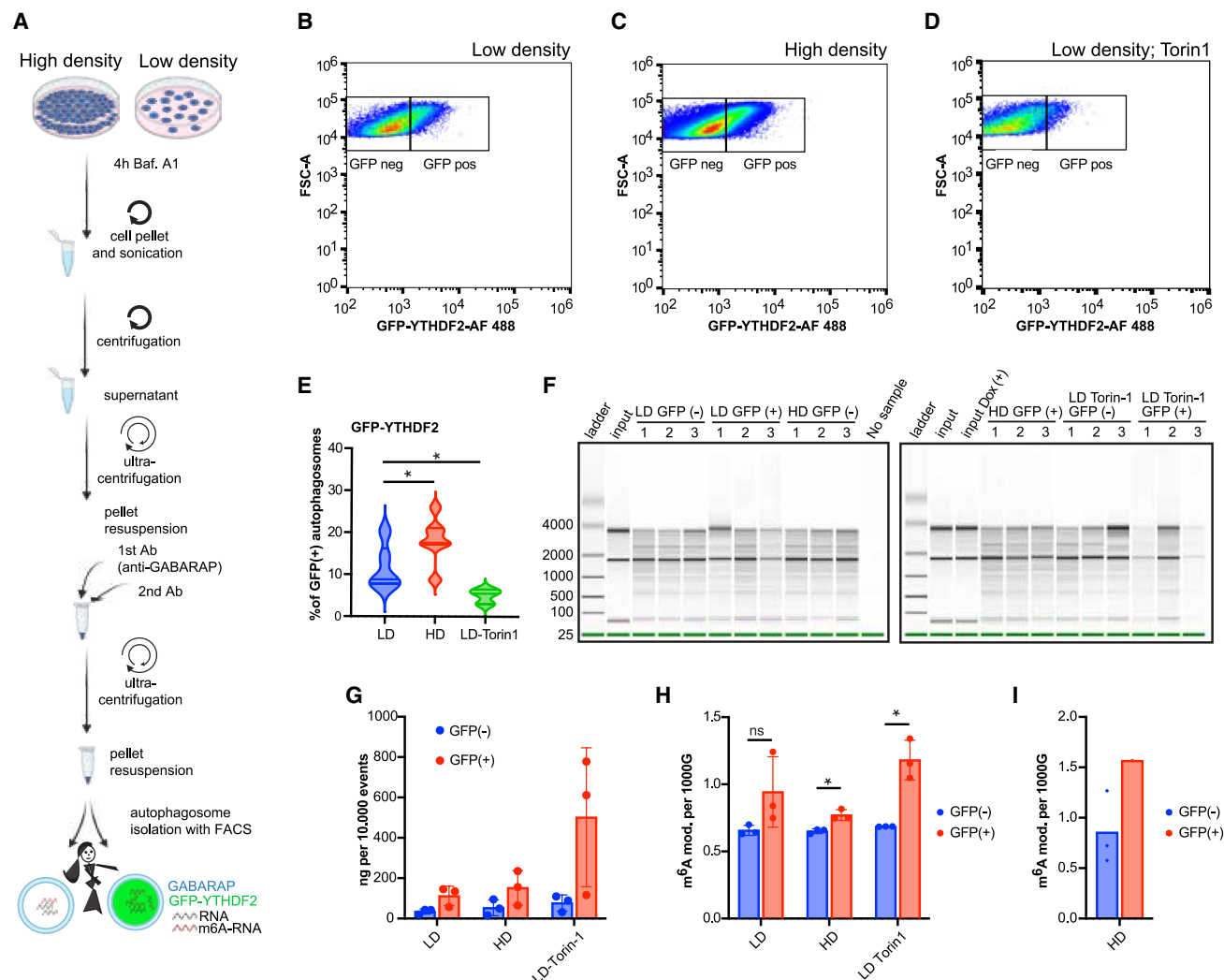


Figure 6. m⁶A RNA is colocalized with YTHDF2 in the autophagosomes

(A) Schematic representation of the antibody (Ab)-based FACS-mediated autophagosome isolation method. RPE1 cells expressing EGFP-YTHDF2-p2A-mCherry were cultured at high and low density. After treatment with bafilomycin A1 (BafA1) for 4 h, cells were collected and lysed in lysis buffer. Supernatant was collected for ultracentrifugation, after which anti-GABARAP Abs (1st Ab) were incubated, followed by anti-rabbit secondary Ab (2nd Ab). Another step of ultracentrifugation was performed, and FACS-based autophagosome isolation was executed. Two populations of autophagosomes were selected, including EGFP positive and negative.

(B–D) Scatterplots of FACS analysis showing GFP-YTHDF2 detection in autophagosomes in low density (B), high density (C), and low density with Torin1 treatment (D).

(E) Quantification of the percentage (%) of GFP-YTHDF2 in autophagosomes in low density, high density, and low density treated with Torin-1. Statistics analysis was calculated using Student's t test (**p* < 0.05) by GraphPad Prism 10.

(F) Bioanalyzer report showing the integrity of RNA isolated from autophagosomes.

(G) Relative normalization of RNA content in autophagosomes.

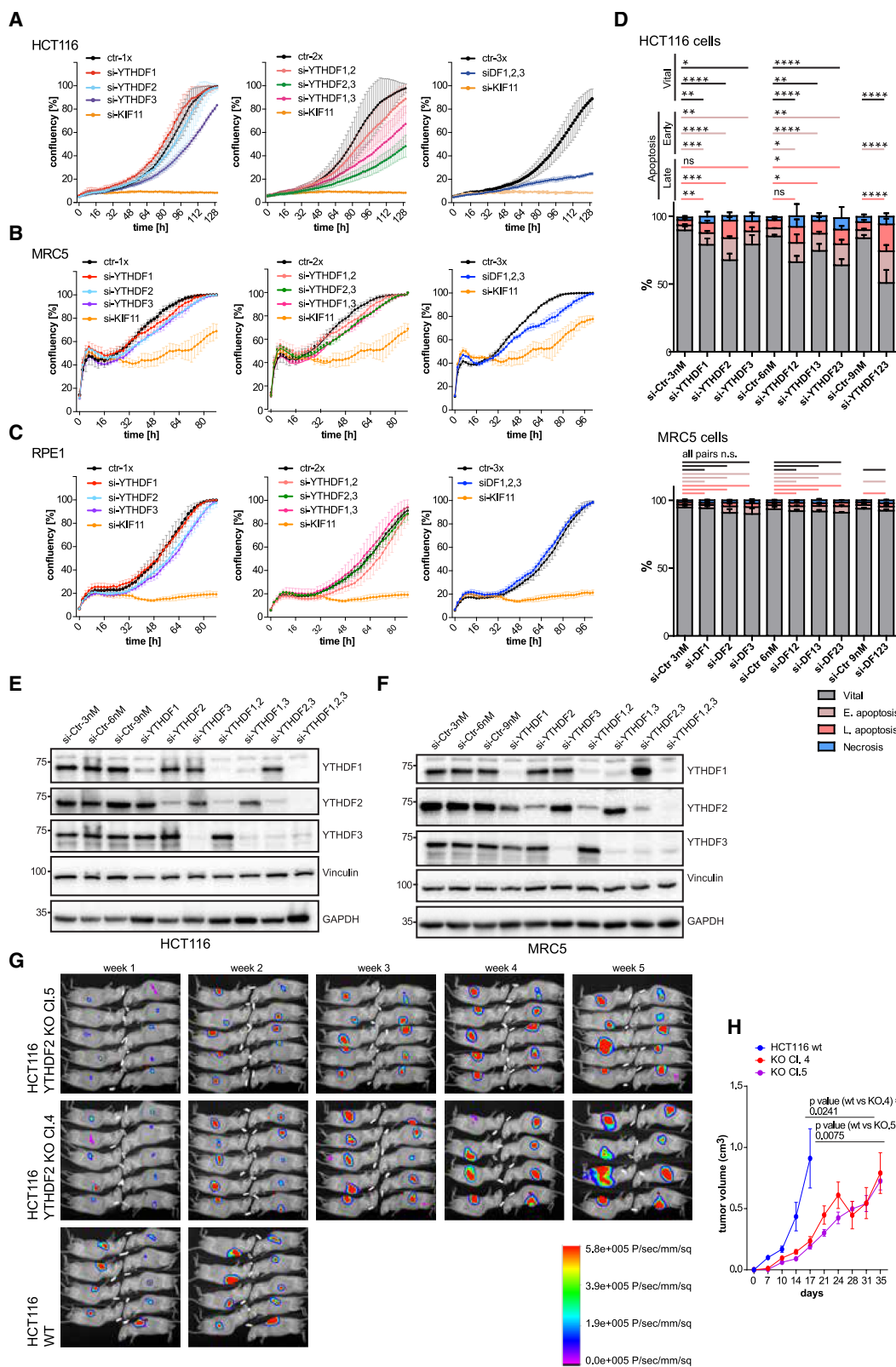
(H and I) Quantification of m⁶A-modified nucleosides in autophagosomes from total RNA (H) and from mRNA isolated from high-density samples (I). Data represent mean with standard deviation (SD). Statistics analysis was calculated using Student's t test by GraphPad Prism 10. **p* < 0.05 and ns, not significant.

(Figures 6G and S8F), suggesting that YTHDF2 facilitates selective RNA incorporation into autophagosomes.

We next quantified m⁶A content using liquid chromatography-tandem mass spectrometry (LC-MS/MS). m⁶A-modified RNA was readily detected in all autophagosomal RNA fractions, with consistent enrichment in EGFP-positive populations (Figure 6H). To further dissect mRNA-specific inclusion, we

depleted rRNA and analyzed the remaining mRNA from pooled HD EGFP-positive samples as well as individual HD EGFP-negative samples. Autophagosomes isolated from HD cultures showed increased m⁶A enrichment in EGFP-positive fractions compared to EGFP-negative controls (Figures 6I and S8G).

Together, these data indicate that YTHDF2 not only undergoes selective autophagic degradation upon contact inhibition but



(legend on next page)

also acts as an RNA-binding autophagy receptor that facilitates the co-degradation of m⁶A-modified RNA. This mechanism provides a rationale for targeting YTHDF2 to autophagosomes: to eliminate both the protein and its bound client RNA as part of a coordinated control mechanism during growth arrest.

YTHDF depletion selectively impairs cancer cell proliferation and induces apoptosis

To determine the functional relevance of YTHDF protein downregulation during contact inhibition and to assess whether cancer cells depend on sustained YTHDF expression, we performed targeted knockdown (KD) experiments using siPOOLS³⁹ against YTHDF1–3 in contact-inhibited (RPE1 and MRC5) and non-contact-inhibited (HCT116) cell lines. Single, double, and triple KDs were carried out, and cell proliferation was quantified in high-throughput 384-well assays (Figures 7A–7C). KIF11 KD served as a positive control to verify transfection efficiency.

In HCT116 cells, single YTHDF KDs led to modest reductions in proliferation, with more pronounced effects observed when metabolism-based proliferation assays were used (Figure S8H). Double KD further impaired growth, and triple KD induced the most severe proliferation defect in HCT116 cells, consistent with functional redundancy among YTHDF proteins (Figure 7A). In contrast, RPE1 cells were largely unaffected across all KD conditions, while MRC5 cells exhibited only a mild growth delay upon triple KD (Figures 7B and 7C). These findings suggest that cancer cells, but not normal proliferating cells, are reliant on high YTHDF protein levels, indicating a potential therapeutic window.

To investigate the basis of the growth defects, we assessed cell cycle progression, apoptosis, and necrosis. FACS analysis revealed that individual YTHDF KDs in HCT116 cells induced G1 arrest (Figure S8I), with YTHDF3 KD producing the most robust block. Interestingly, triple KD did not exacerbate G1 accumulation beyond that observed in double KD, likely due to the selection of partially transfected populations with residual YTHDF expression.

Apoptosis analysis using Annexin V staining demonstrated that all single KDs increased apoptosis in HCT116 cells, with YTHDF2 KD eliciting the strongest effect (Figure 7D, top). Triple KD produced the most significant apoptotic phenotype, reinforcing the model of partial redundancy among YTHDF proteins. Importantly, this pro-apoptotic response was not observed in MRC5 cells, further supporting cancer cell specificity (Figure 7D, bottom).

To evaluate the *in vivo* relevance of these findings, we generated YTHDF2 knockout clones in HCT116.Luc cells using

CRISPR-Cas9 and selected two lines with confirmed protein depletion (Figure S8J). Subcutaneous injection into immunodeficient mice revealed that while tumors formed in all animals, those harboring YTHDF2 knockout cells exhibited delayed growth kinetics compared to wild-type controls, necessitating earlier sacrifice in the wild-type group (Figures 7G and 7H). Taken together, our data revealed that cancer cells rely on high YTHDF protein levels for proliferation, as KD experiments revealed functional redundancy among YTHDF proteins, leading to growth defects, apoptosis, and delayed tumor growth *in vivo*, while normal cells remained largely unaffected.

DISCUSSION

In this study, we identify a previously unrecognized autophagy-dependent mechanism that regulates YTHDF1–3 protein turnover in response to contact inhibition. We show that YTHDF proteins are selectively degraded at high cell density in contact-inhibited, non-transformed cell lines but remain stable in cancer cells that lack this growth control mechanism. This degradation coincides with increased autophagy flux and can be phenocopied by mTOR inhibition using Torin1, linking YTHDF protein stability directly to the mTOR-autophagy axis.

Mechanistically, YTHDF proteins harbor conserved LIR motifs within their disordered N- and C-terminal domains. We identify GABARAP L2 as a selective/preferred binding partner for YTHDF2 and demonstrate that this interaction is mediated through multiple LIR motifs, with LIR1 and LIR8 contributing most strongly. Phosphorylation at S39—adjacent to LIR1—enhances the affinity of YTHDF2 for GABARAP L2 and correlates with YTHDF2 degradation. The sequences of YTHDF1 and YTHDF3 contain an identical LIR motif and a threonine and serine at the respective positions, respectively. Even though it remains to be tested and confirmed, this indicates that phosphorylation close to LIR1 may be a conserved regulatory mechanism between YTHDF family members.

Our data also indicate that YTHDF turnover is dependent on both the UPS²² and autophagy. This is in line with a previous study that reported deactivation of the mTOR signaling pathway upon contact inhibition and HD cells,³⁵ which in turn promotes autophagy. Consistent with this finding, we also observed that autophagy is activated in several contact-inhibited cells but not in cells lacking contact inhibition. The dual degradative pathways highlight the tight regulation of YTHDF abundance, which appears essential for cellular homeostasis. The autophagic

Figure 7. Depletion of YTHDF family members causes cell death in cancer cells

(A–C) Incucyte-based growth data upon YTHDF1/2/3 single (left), double (middle), and triple (right) knockdown in HCT116 (A), MRC5 (B), and RPE1 (C) cells. KIF11 serves as positive control.

(D) Effect of YTHDF protein knockdown in HCT116 cells (top) and MRC5 cells (bottom) on cell apoptosis. The apoptosis analysis was performed 3 days post-transfection using Annexin V staining (*n* = 3); error bars: SD. Statistics analysis was calculated using Student's *t* test by GraphPad Prism 10. **p* < 0.05, ***p* < 0.01, ****p* < 0.001, *****p* < 0.0001, and ns, not significant.

(E and F) Representative western blot analysis of HCT116 cells (E) and MRC5 cells (F) depleted of YTHDF for 3 days using siPOOLS.

(G) *In vivo* bioluminescence monitoring of subcutaneous HCT116.Luc tumors in immunodeficient NSG mice. For bioluminescence imaging, mice were intraperitoneally injected with 150 mg/kg of luciferin and imaged. All mice were sacrificed when bioluminescence levels of the control group reached about 6e10⁵ photons/s. Ten mice were used for this experiment. Notably, tumors in WT mice developed faster, leading to their sacrifice earlier than the corresponding knockout clones.

(H) Tumor volume of the HCT116 WT and two YTHDF2 knockout clones (4 and 5) in immunodeficient mice. Data represent mean with standard error of the mean (SEM). Statistics analysis was calculated by two-way ANOVA using GraphPad Prism 10.

regulation of YTHDF protein levels may also create feedback loops that, in reverse, impact autophagy levels.⁴

The upregulation of YTHDF proteins in various cancers further supports this notion, implicating YTHDF dysregulation in disease progression.^{12,26} The question remains, why do both the UPS and the autophagic systems regulate YTHDF levels under physiological contact inhibition? We show that YTHDF2 is not only a substrate of autophagy but could also guide m⁶A-modified RNA for autophagic degradation. Using autophagosome isolation and m⁶A quantification, we demonstrate that YTHDF2-positive autophagosomes are enriched in total and m⁶A-modified RNA, suggesting that YTHDF2 mediates the co-sequestration of its RNA clients into autophagosomes. This autophagic RNA degradation could, however, be a simple bystander effect of a fast depletion of YTHDF proteins: free (RNA-unbound) YTHDF is degraded by the proteasome, and YTHDF in complex with RNA is simultaneously targeted by the autophagic machinery. The other possibility is that YTHDF proteins serve as selective autophagy receptors to constitutively deplete specific RNA pools (e.g., needed for proliferation) in a contact-inhibited state. Such a function would echo mechanisms observed in yeast, where selective mRNA degradation via autophagy contributes to gene expression remodeling under stress,^{40,41} and explain why YTHDF proteins are regulated on the protein and not on the gene level. Such pathways could affect individual mRNAs, larger mRNP structures, or even phase-separated structures, such as P bodies and stress granules.⁴²

Last but not least, the constitutive turnover of YTHDF proteins together with mRNA clients may serve as a quality control pathway that ensures depletion of any available m⁶A-modified mRNA. A YTHDF-dependent stress response pathway upon repressed translation has recently been reported.⁴³ This is in the same line as a report that the turnover of an m⁶A-containing transcript depends on the translation.⁴⁴ It could well be that under certain conditions—e.g., contact inhibition, where translation is also reduced—selective autophagy of YTHDF proteins and their m⁶A-modified mRNA may prevent the reported accumulation of m⁶A-modified RNAs and therefore suppress an unwanted activation of stress response pathways.

In conclusion, our findings have broader implications for understanding how cells coordinate protein and RNA turnover in response to growth signals. Contact inhibition, a key anti-proliferative mechanism, appears to utilize this pathway to reduce levels of both YTHDF proteins and their target RNAs, potentially promoting differentiation or quiescence.⁴⁵

Cancer cells that escape contact inhibition retain high YTHDF levels, thereby preserving m⁶A-modified RNA pools that may support continued proliferation.⁴⁶ Depletion of YTHDF proteins in HCT116 cancer cells induces cell-cycle arrest and apoptosis, both *in vitro* and in xenograft models. These findings establish a functional requirement for YTHDF proteins in cancer cell survival, particularly for YTHDF2. The absence of similar phenotypes in non-transformed cells highlights the selective vulnerability of cancer cells to YTHDF depletion and underscores their potential as therapeutic targets in malignancy.

Limitation of this study

This study demonstrates autophagic regulation of YTHDF proteins and associated m⁶A-modified RNAs. Several interesting

yet open aspects are worth following up with in future research. In particular, the following points limit the conclusions that can be drawn from the current dataset: (1) the number of biological processes in which autophagic downregulation of YTHDF levels is taking place is currently unknown and will probably exceed contact inhibition. (2) Probably more proteins than just the three YTHDF family members will be targeted by the autophagic pathways that are activated upon the onset of contact inhibition, which exactly remains to be studied. (3) While we report the induction of autophagy upon the onset of contact inhibition, this study does not provide a detailed analysis of the autophagic state of contact-inhibited cells and the (in)activation of known selective autophagy receptors. (4) The current dataset does not allow a final conclusion regarding the functional relevance of the reported autophagic regulation of YTHDF proteins. For example, the detailed analysis of which m⁶A-modified RNAs are targeted by autophagy and whether these RNAs are related to contact inhibition remains open.

We apologize to all the scientists whose precious work about, e.g., YTHDF functions, m⁶A modification, contact inhibition, cancer, and autophagy was not cited in this manuscript due to space limitations.

RESOURCE AVAILABILITY

Lead contact

Further information and requests may be directed to the lead contact, Alexandra Stolz (stolz@em.uni-frankfurt.de), or directly to the institution indicated in the [key resources table](#).

Materials availability

All unique/stable reagents generated in this study are available from the lead contact with a completed materials transfer agreement.

Data and code availability

Data reported in this paper will be shared by the [lead contact](#) upon request, except for the original images of Incucyte screens due to the large file size (processed metadata are available).

ACKNOWLEDGMENTS

We thank S. Ammon, C. Friederich, and G. Lehmann for excellent technical support and Balagopal Pai, Markus Kretz, Rayene Berkane, Thorsten Mosler, and Christina Hackl for discussion. We are thankful to Sam Ringle, Franziska Weichmann, and Eva Schöller for support with monoclonal anti-YTHDF2 antibody validation. We are grateful to Laura Manelyte (University of Regensburg, Germany), Martin Ehrenschröder (University Hospital Regensburg, Germany), Anders Lund (BRIC, Copenhagen, Denmark), and Joachim Wegener (University of Regensburg, Germany) for providing cells. We thank Gerhard Plendl, Stephanie Blaimer, and Gero Brockhoff (University Hospital Regensburg, Germany) for helping with FACS analysis of the cell cycle and apoptosis and João Mello-Vieira (Goethe University Frankfurt, Germany) and Pascale Henning-Domres (Johannes Gutenberg University Mainz, Germany) for helping with FACS-based autophagosome isolation. This work was funded by the Boehringer Ingelheim Foundation (Exploration grant to A.S.); the Deutsche Forschungsgemeinschaft (DFG, German Research Foundation) – grant numbers 242727105 (FOR2127) to G.M., 259130777 (SFB1177) to S.K. and A.S., 514894665 (TRR 387/1) to I.D. and A.S., 515275293 (FuGG; cell sorter), and 512574446 (FuGG; spinning disc confocal); the Bayerische Forschungsförderung (FORTiTher) to G.M.; and the Hessian Ministry for Science and the Arts (HMWK; project ENABLE) to V.D., G.H., and A.S. The Czech Centre for Phenogenomics at the Institute of Molecular Genetics was supported by the Czech Academy of Sciences RVO 68378050 and by project LM2023036

provided by the Ministry of Education, Youth and Sports of the Czech Republic. J.F.M.S. and G.H. thank the Max Planck Society for financial support and the Max Planck Computing and Data Facility for computational resources.

AUTHOR CONTRIBUTIONS

Conceptualization, H.H.-X., G.M., and A.S.; methodology, H.H.-X., C.P.-G., J. F.M.S., L.B., A.V., A.P., H.W., A.K., A.-C.J., J.P., R.F., V.D., R.S., G.H., S.K., I. D., G.M., and A.S.; formal analysis, H.H.-X., L.N., C.P.-G., J.F.M.S., L.B., A.V., A.P., H.W., A.K., P.S.-M., B.d.I.C.-T., J.P., G.M., and A.S.; validation, H.H.-X., G.M., and A.S.; data curation, H.H.-X., L.B., S.C.-F., J.P., G.M., and A.S.; visualization, H.H.-X., G.M., and A.S.; writing – original draft, H.H.-X. and A.S.; writing – review & editing, I.D. and G.M.; investigation, A.B., L.N., C.P.-G., J. F.M.S., L.B., A.P., S.C.-F., S.L., P.S.-M., B.d.I.C.-T., A.-C.J., J.P., R.F., V.D., and M.M.M.; resources, A.B., S.L., R.F., V.D., R.S., G.H., S.K., I.D., and M. M.M.; funding acquisition, R.S., G.H., S.K., G.M., and A.S.; supervision, G. H., S.K., I.D., M.M.M., G.M., and A.S.; project administration, G.M. and A.S.

DECLARATION OF INTERESTS

The authors do not declare any conflict of interest related to this work.

DECLARATION OF GENERATIVE AI AND AI-ASSISTED TECHNOLOGIES IN THE WRITING PROCESS

During the preparation of this work, the authors used ChatGPT for text editing of the prefinal manuscript. After using this tool/service, the authors reviewed and edited the content as needed and take full responsibility for the content of the publication.

STAR★METHODS

Detailed methods are provided in the online version of this paper and include the following:

- **KEY RESOURCES TABLE**
- **EXPERIMENTAL MODEL AND STUDY PARTICIPANT DETAILS**
 - Cell lines
 - Animal models for the development of monoclonal antibodies against YTHDF2
 - *In vivo* experiments for myc-related experiments
 - Hydrodynamic tail-vein injection
 - Xenograft
 - Human participants
- **METHOD DETAILS**
 - Plasmids, antibodies and siPOOLS
 - Generation of a monoclonal antibody against YTHDF2
 - Cell culture and generation of stable cell lines
 - Generation of protein lysates and western blot analyses
 - Co-immunoprecipitation (Co-IP)
 - Proliferation assay
 - Cell cycle analysis
 - Apoptosis analysis
 - Ribosome immunoprecipitation followed by qPCR (Ribo-IP-qPCR)
 - RNA preparation, qPCR, and northern blot analysis
 - Autophagy flux assay
 - Immunofluorescence
 - Analysis of publicly available human datasets
 - Autophagosome isolation
 - Total RNA isolation
 - mRNA enrichment
 - RNA digestion
 - Nucleoside mass spectrometry
 - Quantification of nucleosides
 - Immunoprecipitation (IP) of endogenous YTHDF2
 - SRM-quantification of phosphorylated peptides
 - Multiple sequence alignment and conservation scores

- Sequence-based LIR prediction
- AlphaFold modeling and LIR prediction
- Molecular dynamics simulations
- Isothermal titration calorimetry (ITC)
- **QUANTIFICATION AND STATISTICAL ANALYSIS**

SUPPLEMENTAL INFORMATION

Supplemental information can be found online at <https://doi.org/10.1016/j.celrep.2025.116188>.

Received: May 23, 2024

Revised: April 15, 2025

Accepted: August 1, 2025

Published: August 23, 2025

REFERENCES

1. Yamamoto, H., Zhang, S., and Mizushima, N. (2023). Autophagy genes in biology and disease. *Nat. Rev. Genet.* 24, 382–400. <https://doi.org/10.1038/s41576-022-00562-w>.
2. Dikic, I., and Elazar, Z. (2018). Mechanism and medical implications of mammalian autophagy. *Nat. Rev. Mol. Cell Biol.* 19, 349–364. <https://doi.org/10.1038/s41580-018-0003-4>.
3. Johansen, T., and Lamark, T. (2020). Selective Autophagy: ATG8 Family Proteins, LIR Motifs and Cargo Receptors. *J. Mol. Biol.* 432, 80–103. <https://doi.org/10.1016/j.jmb.2019.07.016>.
4. Abildgaard, M.H., Brynjólfssdóttir, S.H., and Frankel, L.B. (2020). The Autophagy-RNA Interplay: Degradation and Beyond. *Trends Biochem. Sci.* 45, 845–857. <https://doi.org/10.1016/j.tibs.2020.07.007>.
5. Murakami, S., and Jaffrey, S.R. (2022). Hidden codes in mRNA: Control of gene expression by m6A. *Mol. Cell* 82, 2236–2251. <https://doi.org/10.1016/j.molcel.2022.05.029>.
6. Frye, M., Harada, B.T., Behm, M., and He, C. (2018). RNA modifications modulate gene expression during development. *Science* 361, 1346–1349. <https://doi.org/10.1126/science.aau1646>.
7. Schöller, E., Weichmann, F., Treiber, T., Ringle, S., Treiber, N., Flatley, A., Feederle, R., Bruckmann, A., and Meister, G. (2018). Interactions, localization, and phosphorylation of the m6A generating METTL3-METTL14-WTAP complex. *RNA* 24, 499–512. <https://doi.org/10.1261/ma.064063.117>.
8. Wang, X., Feng, J., Xue, Y., Guan, Z., Zhang, D., Liu, Z., Gong, Z., Wang, Q., Huang, J., Tang, C., et al. (2016). Structural basis of N(6)-adenosine methylation by the METTL3-METTL14 complex. *Nature* 534, 575–578. <https://doi.org/10.1038/nature18298>.
9. Wang, X., Lu, Z., Gomez, A., Hon, G.C., Yue, Y., Han, D., Fu, Y., Parisien, M., Dai, Q., Jia, G., et al. (2014). N6-methyladenosine-dependent regulation of messenger RNA stability. *Nature* 505, 117–120. <https://doi.org/10.1038/nature12730>.
10. Śledź, P., and Jinek, M. (2016). Structural insights into the molecular mechanism of the m(6)A writer complex. *eLife* 5. <https://doi.org/10.7554/eLife.18434>.
11. Destefanis, E., Sighel, D., Dalfovo, D., Gilmozzi, R., Broso, F., Cappannini, A., Bujnicki, J.M., Romanel, A., Dassi, E., and Quattrone, A. (2024). The three YTHDF paralogs and VIRMA are strong cross-histotype tumor driver candidates among m6A core genes. *NAR cancer* 6, zcae040. <https://doi.org/10.1093/narcan/zcae040>.
12. Delaunay, S., and Frye, M. (2019). RNA modifications regulating cell fate in cancer. *Nat. Cell Biol.* 21, 552–559. <https://doi.org/10.1038/s41556-019-0319-0>.
13. Liu, N., Dai, Q., Zheng, G., He, C., Parisien, M., and Pan, T. (2015). N(6)-methyladenosine-dependent RNA structural switches regulate RNA-protein interactions. *Nature* 518, 560–564. <https://doi.org/10.1038/nature14234>.

14. Alarcón, C.R., Goodarzi, H., Lee, H., Liu, X., Tavazoie, S., and Tavazoie, S. F. (2015). HNRNPA2B1 Is a Mediator of m(6)A-Dependent Nuclear RNA Processing Events. *Cell* 162, 1299–1308. <https://doi.org/10.1016/j.cell.2015.08.011>.
15. Zhang, F., Kang, Y., Wang, M., Li, Y., Xu, T., Yang, W., Song, H., Wu, H., Shu, Q., and Jin, P. (2018). Fragile X mental retardation protein modulates the stability of its m6A-marked messenger RNA targets. *Hum. Mol. Genet.* 27, 3936–3950. <https://doi.org/10.1093/hmg/ddy292>.
16. Huang, H., Weng, H., Sun, W., Qin, X., Shi, H., Wu, H., Zhao, B.S., Mesquita, A., Liu, C., Yuan, C.L., et al. (2018). Recognition of RNA N6-methyladenosine by IGF2BP proteins enhances mRNA stability and translation. *Nat. Cell Biol.* 20, 285–295. <https://doi.org/10.1038/s41556-018-0045-z>.
17. Patil, D.P., Pickering, B.F., and Jaffrey, S.R. (2018). Reading m6A in the Transcriptome: m6A-Binding Proteins. *Trends Cell Biol.* 28, 113–127. <https://doi.org/10.1016/j.tcb.2017.10.001>.
18. Zaccara, S., and Jaffrey, S.R. (2020). A Unified Model for the Function of YTHDF Proteins in Regulating m6A-Modified mRNA. *Cell* 181, 1582–1595.e18. <https://doi.org/10.1016/j.cell.2020.05.012>.
19. Lasman, L., Krupalnik, V., Viukov, S., Mor, N., Aguilera-Castrejon, A., Schner, D., Bayerl, J., Mizrahi, O., Peles, S., Tawil, S., et al. (2020). Context-dependent compensation between functional Ythdf m6A reader proteins. *Genes Dev.* 34, 1373–1391. <https://doi.org/10.1101/gad.340695.120>.
20. Wang, X., Zhao, B.S., Roundtree, I.A., Lu, Z., Han, D., Ma, H., Weng, X., Chen, K., Shi, H., and He, C. (2015). N(6)-methyladenosine Modulates Messenger RNA Translation Efficiency. *Cell* 161, 1388–1399. <https://doi.org/10.1016/j.cell.2015.05.014>.
21. Xiao, W., Adhikari, S., Dahal, U., Chen, Y.-S., Hao, Y.-J., Sun, B.-F., Sun, H.-Y., Li, A., Ping, X.-L., Lai, W.-Y., et al. (2016). Nuclear m(6)A Reader YTHDC1 Regulates mRNA Splicing. *Mol. Cell* 61, 507–519. <https://doi.org/10.1016/j.molcel.2016.01.012>.
22. Fei, Q., Zou, Z., Roundtree, I.A., Sun, H.-L., and He, C. (2020). YTHDF2 promotes mitotic entry and is regulated by cell cycle mediators. *PLoS Biol.* 18, e3000664. <https://doi.org/10.1371/journal.pbio.3000664>.
23. Fang, R., Chen, X., Zhang, S., Shi, H., Ye, Y., Shi, H., Zou, Z., Li, P., Guo, Q., Ma, L., et al. (2021). EGFR/SRC/ERK-stabilized YTHDF2 promotes cholesterol dysregulation and invasive growth of glioblastoma. *Nat. Commun.* 12, 177. <https://doi.org/10.1038/s41467-020-20379-7>.
24. Abercrombie, M. (1979). Contact inhibition and malignancy. *Nature* 281, 259. <https://doi.org/10.1038/281259a0>.
25. McClatchey, A.I., and Yap, A.S. (2012). Contact inhibition (of proliferation) redux. *Curr. Opin. Cell Biol.* 24, 685–694. <https://doi.org/10.1016/j.ccb.2012.06.009>.
26. Zhang, W., Wu, T., Zhang, Y., Kang, W., Du, C., You, Q., Chen, X., and Jiang, Z. (2023). Targeting m6A binding protein YTHDFs for cancer therapy. *Bioorg. Med. Chem.* 90, 117373. <https://doi.org/10.1016/j.bmc.2023.117373>.
27. Tang, Z., Kang, B., Li, C., Chen, T., and Zhang, Z. (2019). GEPIA2: an enhanced web server for large-scale expression profiling and interactive analysis. *Nucleic Acids Res.* 47, W556–W560. <https://doi.org/10.1093/nar/gkz430>.
28. Llombart, V., and Mansour, M.R. (2022). Therapeutic targeting of “undrugable” MYC. *EBioMedicine* 75, 103756. <https://doi.org/10.1016/j.ebiom.2021.103756>.
29. Einstein, J.M., Perelis, M., Chaim, I.A., Meena, J.K., Nussbacher, J.K., Tankka, A.T., Yee, B.A., Li, H., Madrigal, A.A., Neill, N.J., et al. (2021). Inhibition of YTHDF2 triggers proteotoxic cell death in MYC-driven breast cancer. *Mol. Cell* 81, 3048–3064.e9. <https://doi.org/10.1016/j.molcel.2021.06.014>.
30. Hengst, L., and Reed, S.I. (1996). Translational control of p27Kip1 accumulation during the cell cycle. *Science* 271, 1861–1864. <https://doi.org/10.1126/science.271.5257.1861>.
31. Kang, S., Antoniewicz, M.R., and Hay, N. (2024). Metabolic and transcriptional reprogramming during contact inhibition-induced quiescence is mediated by YAP-dependent and YAP-independent mechanisms. *Nat. Commun.* 15, 6777. <https://doi.org/10.1038/s41467-024-51117-y>.
32. Kaizuka, T., Morishita, H., Hama, Y., Tsukamoto, S., Matsui, T., Toyota, Y., Kodama, A., Ishihara, T., Mizushima, T., and Mizushima, N. (2016). An Autophagic Flux Probe that Releases an Internal Control. *Mol. Cell* 64, 835–849. <https://doi.org/10.1016/j.molcel.2016.09.037>.
33. Cano-Franco, S., Ho-Xuan, H., Brunello, L., and Stolz, A. (2023). Live-Cell High-Throughput Screen for Monitoring Autophagy Flux. *Methods Mol. Biol.* 2706, 215–224. https://doi.org/10.1007/978-1-0716-3397-7_16.
34. Kalvari, I., Tsompanis, S., Mulakkal, N.C., Osgood, R., Johansen, T., Nezis, I.P., and Promponas, V.J. (2014). iLIR: A web resource for prediction of Atg8-family interacting proteins. *Autophagy* 10, 913. <https://doi.org/10.4161/auto.28260>.
35. Leontieva, O.V., Demidenko, Z.N., and Blagosklonny, M.V. (2014). Contact inhibition and high cell density deactivate the mammalian target of rapamycin pathway, thus suppressing the senescence program. *Proc. Natl. Acad. Sci. USA* 111, 8832–8837. <https://doi.org/10.1073/pnas.1405723111>.
36. Li, J., Van Vranken, J.G., Pontano Vaite, L., Schweppe, D.K., Huttlin, E.L., Etienne, C., Nandhikonda, P., Viner, R., Robitaille, A.M., Thompson, A.H., et al. (2020). TMTpro reagents: a set of isobaric labeling mass tags enables simultaneous proteome-wide measurements across 16 samples. *Nat. Methods* 17, 399–404. <https://doi.org/10.1038/s41592-020-0781-4>.
37. Wild, P., Farhan, H., McEwan, D.G., Wagner, S., Rogov, V.V., Brady, N.R., Richter, B., Korac, J., Waidmann, O., Choudhary, C., et al. (2011). Phosphorylation of the autophagy receptor optineurin restricts Salmonella growth. *Science* 333, 228–233. <https://doi.org/10.1126/science.1205405>.
38. Schmitt, D., Bozkurt, S., Henning-Domres, P., Huesmann, H., Eimer, S., Bindila, L., Behrends, C., Boyle, E., Wilfling, F., Tascher, G., et al. (2022). Lipid and protein content profiling of isolated native autophagic vesicles. *EMBO Rep.* 23, e53065. <https://doi.org/10.15252/embr.202153065>.
39. Hannus, M., Beitzinger, M., Engelmann, J.C., Weickert, M.-T., Spang, R., Hannus, S., and Meister, G. (2014). siPools: highly complex but accurately defined siRNA pools eliminate off-target effects. *Nucleic Acids Res.* 42, 8049–8061. <https://doi.org/10.1093/nar/gku480>.
40. Makino, S., Kawamata, T., Iwasaki, S., and Ohsumi, Y. (2021). Selectivity of mRNA degradation by autophagy in yeast. *Nat. Commun.* 12, 2316. <https://doi.org/10.1038/s41467-021-22574-6>.
41. Huang, H., Kawamata, T., Horie, T., Tsugawa, H., Nakayama, Y., Ohsumi, Y., and Fukusaki, E. (2015). Bulk RNA degradation by nitrogen starvation-induced autophagy in yeast. *EMBO J.* 34, 154–168. <https://doi.org/10.15252/emboj.201489083>.
42. Chen, Y., Wan, R., Zou, Z., Lao, L., Shao, G., Zheng, Y., Tang, L., Yuan, Y., Ge, Y., He, C., and Lin, S. (2023). O-GlcNAcylation determines the translational regulation and phase separation of YTHDF proteins. *Nat. Cell Biol.* 25, 1676–1690. <https://doi.org/10.1038/s41556-023-01258-x>.
43. Murakami, S., Olarerin-George, A.O., Liu, J.F., Zaccara, S., Hawley, B., and Jaffrey, S.R. (2025). m6A alters ribosome dynamics to initiate mRNA degradation. *Cell* 188, 3728–3743.e20. <https://doi.org/10.1016/j.cell.2025.04.020>.
44. Zhou, Y., Ćorović, M., Hoch-Kraft, P., Meiser, N., Mesitov, M., Körtel, N., Back, H., Naarmann-de Vries, I.S., Katti, K., Obrdlík, A., et al. (2024). m6A sites in the coding region trigger translation-dependent mRNA decay. *Mol. Cell* 84, 4576–4593.e12. <https://doi.org/10.1016/j.molcel.2024.10.033>.
45. de la Cruz-Thea, B., Natali, L., Ho-Xuan, H., Bruckmann, A., Coll-Bonfill, N., Strieder, N., Peinado, V.I., Meister, G., and Musri, M.M. (2024). Differentiation and Growth-Arrest-Related lncRNA (DAGAR): Initial Characterization in Human Smooth Muscle and Fibroblast Cells. *Int. J. Mol. Sci.* 25, 9497. <https://doi.org/10.3390/ijms25179497>.

46. An, Y., and Duan, H. (2022). The role of m6A RNA methylation in cancer metabolism. *Mol. Cancer* 21, 14. <https://doi.org/10.1186/s12943-022-01500-4>.
47. Diehl, V., Wegner, M., Grumati, P., Husnjak, K., Schaubek, S., Gubas, A., Shah, V.J., Polat, I.H., Langschied, F., Prieto-Garcia, C., et al. (2021). Minimized combinatorial CRISPR screens identify genetic interactions in autophagy. *Nucleic Acids Res.* 49, 5684–5704. <https://doi.org/10.1093/nar/gkab309>.
48. Beckers, A., and Bazin, H.J. (1978). Incidence of spontaneous ileocecal immunocytomas in hybrids of LOU/C rats and rat strains with low spontaneous tumor incidence. *Natl Cancer Inst.* 60, 1505. <https://doi.org/10.1093/jnci/60.6.1505>.
49. Pan, D., Klare, K., Petrovic, A., Take, A., Walstein, K., Singh, P., Rondelet, A., Bird, A.W., and Musacchio, A. (2017). CDK-regulated dimerization of M18BP1 on a Mis18 hexamer is necessary for CENP-A loading. *eLife* 6, e23352. <https://doi.org/10.7554/eLife.23352>.
50. Kuznetsov, D., Tegenfeldt, F., Manni, M., Seppey, M., Berkeley, M., Kriventseva, E.V., and Zdobnov, E.M. (2023). OrthoDB v11: annotation of orthologs in the widest sampling of organismal diversity. *Nucleic Acids Res.* 51, D445–D451. <https://doi.org/10.1093/nar/gkac998>.
51. Edgar, R.C. (2004). MUSCLE: multiple sequence alignment with high accuracy and high throughput. *Nucleic Acids Res.* 32, 1792–1797. <https://doi.org/10.1093/nar/gkh340>.
52. Capra, J.A., and Singh, M. (2007). Predicting functionally important residues from sequence conservation. *Bioinformatics* 23, 1875–1882. <https://doi.org/10.1093/bioinformatics/btm270>.
53. Jumper, J., Evans, R., Pritzel, A., Green, T., Figurnov, M., Ronneberger, O., Tunyasuvunakool, K., Bates, R., Židek, A., Potapenko, A., et al. (2021). Highly accurate protein structure prediction with AlphaFold. *Nature* 596, 583–589. <https://doi.org/10.1038/s41586-021-03819-2>.
54. Stuke, J.F.M., and Hummer, G. (2024). AlphaFold2 SLiM screen for LC3-LIR interactions in autophagy. <https://doi.org/10.1101/2024.09.06.611604>.
55. Abramson, J., Adler, J., Dunger, J., Evans, R., Green, T., Pritzel, A., Ronneberger, O., Willmore, L., Ballard, A.J., Bambrick, J., et al. (2024). Accurate structure prediction of biomolecular interactions with AlphaFold 3. *Nature* 630, 493–500. <https://doi.org/10.1038/s41586-024-07487-w>.
56. Huang, J., Rauscher, S., Nawrocki, G., Ran, T., Feig, M., de Groot, B.L., Grubmüller, H., and MacKerell, A.D. (2017). CHARMM36m: an improved force field for folded and intrinsically disordered proteins. *Nat. Methods* 14, 71–73. <https://doi.org/10.1038/nmeth.4067>.
57. Michaud-Agrawal, N., Denning, E.J., Woolf, T.B., and Beckstein, O. (2011). MDAAnalysis: a toolkit for the analysis of molecular dynamics simulations. *J. Comput. Chem.* 32, 2319–2327. <https://doi.org/10.1002/jcc.21787>.
58. Humphrey, W., Dalke, A., and Schulten, K. (1996). VMD: Visual molecular dynamics. *J. Mol. Graph.* 14, 33. [https://doi.org/10.1016/0263-7855\(96\)00018-5](https://doi.org/10.1016/0263-7855(96)00018-5).
59. Keller, S., Vargas, C., Zhao, H., Piszczek, G., Brautigam, C.A., and Schuck, P. (2012). High-precision isothermal titration calorimetry with automated peak-shape analysis. *Anal. Chem.* 84, 5066–5073. <https://doi.org/10.1021/ac3007522>.
60. Houtman, J.C.D., Brown, P.H., Bowden, B., Yamaguchi, H., Appella, E., Samelson, L.E., and Schuck, P. (2007). Studying multisite binary and ternary protein interactions by global analysis of isothermal titration calorimetry data in SEDPHAT: application to adaptor protein complexes in cell signaling. *Protein Sci.* 16, 30–42. <https://doi.org/10.1110/ps.062558507>.
61. Brautigam, C.A. (2015). Calculations and Publication-Quality Illustrations for Analytical Ultracentrifugation Data. *Methods Enzymol.* 562, 109–133. <https://doi.org/10.1016/bs.mie.2015.05.001>.
62. Herhaus, L., Gestal-Mato, U., Eapen, V.V., Mačinković, I., Bailey, H.J., Prieto-Garcia, C., Misra, M., Jacomin, A.-C., Ammanath, A.V., Bagarić, I., et al. (2024). IRGQ-mediated autophagy in MHC class I quality control promotes tumor immune evasion. *Cell* 187, 7285–7302.e29. <https://doi.org/10.1016/j.cell.2024.09.048>.
63. Ho-Xuan, H., Glazar, P., Latini, C., Heizler, K., Haase, J., Hett, R., Anders, M., Weichmann, F., Bruckmann, A., Van den Berg, D., et al. (2020). Comprehensive analysis of translation from overexpressed circular RNAs reveals pervasive translation from linear transcripts. *Nucleic Acids Res.* 48, 10368–10382. <https://doi.org/10.1093/nar/gkaa704>.
64. Györfy, B. (2024). Transcriptome-level discovery of survival-associated biomarkers and therapy targets in non-small-cell lung cancer. *Br. J. Pharmacol.* 181, 362–374. <https://doi.org/10.1111/bph.16257>.
65. Bartha, Á., and Györfy, B. (2021). TNMplot.com: A Web Tool for the Comparison of Gene Expression in Normal, Tumor and Metastatic Tissues. *Int. J. Mol. Sci.* 22. <https://doi.org/10.3390/ijms22052622>.
66. Fekete, J.T., and Györfy, B. (2019). ROCplot.org: Validating predictive biomarkers of chemotherapy/hormonal therapy/anti-HER2 therapy using transcriptomic data of 3,104 breast cancer patients. *Int. J. Cancer* 145, 3140–3151. <https://doi.org/10.1002/ijc.32369>.
67. Evans, R., O'Neill, M., Pritzel, A., Antropova, N., Senior, A., Green, T., Židek, A., Bates, R., Blackwell, S., Yim, J., et al. (2021). Protein complex prediction with AlphaFold-Multimer. Preprint at bioRxiv. <https://doi.org/10.1101/2021.10.04.463034>.
68. Abraham, M.J., Murtola, T., Schulz, R., Páll, S., Smith, J.C., Hess, B., and Lindahl, E. (2015). GROMACS: High performance molecular simulations through multi-level parallelism from laptops to supercomputers. *SoftwareX* 1–2, 19–25. <https://doi.org/10.1016/j.softx.2015.06.001>.

STAR★METHODS

KEY RESOURCES TABLE

REAGENT or RESOURCE	SOURCE	IDENTIFIER
Antibodies		
Rabbit polyclonal anti-YTHDF1	ProteinTech	Cat#17479-1-AP; RRID: AB_2217473
Rabbit polyclonal anti-YTHDF2	ProteinTech	Cat#24744-1-AP; RRID: AB_2687435
Rat monoclonal anti-YTHDF2 clone 9G1	This study, Helmholtz Munich	na
Mouse monoclonal anti-YTHDF2 clone 32A11	This study, Helmholtz Munich	na
Rabbit polyclonal anti-YTHDF3	ProteinTech	Cat#25537-1-AP; RRID: AB_2847817
Mouse monoclonal anti-YTHDF3	Santa Cruz Biotechnology	Cat#sc-377119; RRID:AB_2687436
Rabbit polyclonal anti-beta-Tubulin	Abcam	Cat#ab6046; RRID:AB_2210370
Mouse monoclonal anti-GAPDH	GeneTex	Cat#GTX627408; RRID:AB_11174761
Rabbit monoclonal anti-p27	Cell Signaling Technology	Cat#3686S; RRID:AB_2077850
Rabbit polyclonal anti-LC3A/B	Cell Signaling Technology	Cat#4108S; RRID:AB_2137703
Rabbit polyclonal anti-LC3 pAb	MBL Life Sciences	Cat#PM036; RRID:AB_2274121
Mouse monoclonal anti-CDK6	Santa Cruz Biotechnology	Cat#sc-7961; RRID:AB_627242
Rabbit monoclonal anti-CDK6	Abcam	Cat#EPR4515; RRID:AB_10999714
Rabbit monoclonal anti-HA	Cell Signaling Technology	Cat#3724T; RRID: AB_1549585
Mouse monoclonal anti-Vinculin	Sigma-Aldrich	Cat#V4505; RRID:AB_477617
Anti-REEP5	Santa Cruz Biotechnology	Cat#sc-393508; RRID: N/A
Rabbit monoclonal anti-c-Myc	Cell Signaling Technology	Cat#5605S; RRID: AB_1903938
Rabbit monoclonal anti-Myc tag 71D10	Cell Signaling Technology	Cat#2278S; RRID:AB_490778
Rabbit polyclonal anti-Phospho-p70 S6 Kinase (Thr421/Ser424)	Cell Signaling Technology	Cat#9204S; RRID:AB_2265913
Rabbit polyclonal anti-Phospho-p70 S6 Kinase (Thr389)	Cell Signaling Technology	Cat# 9205S; RRID:AB_330944
Rabbit polyclonal anti-p70 S6 Kinase Antibody	Cell Signaling Technology	Cat#9202S; RRID:AB_331676
Rabbit polyclonal anti-RPS3	ProteinTech	Cat#11990-1-AP; RRID:AB_2180758
Rabbit monoclonal anti-GABARAP antibody	Abcam	Cat#ab109364; RRID:AB_10861928
Goat polyclonal anti-Rabbit IgG, IRDye 800CW conjugated antibody	LI-COR Biosciences	Cat#926-32211; RRID: AB_621843
Goat polyclonal anti-mouse IgG, IRDye 800CW conjugated antibody	LI-COR Biosciences	Cat#925-32210; RRID: AB_2687825
Goat polyclonal anti-rat IgG, IRDye 800CW conjugated antibody	LI-COR Biosciences	Cat#926-32219; RRID: AB_1850025
Goat anti-rabbit IgG, IRDye 680RD conjugated antibody	LI-COR Biosciences	Cat#926-68071, RRID: AB_10956166
Goat anti-mouse IgG, IRDye 680RD conjugated antibody	LI-COR Biosciences	Cat#926-68070; RRID: AB_10956588
Goat anti-rat IgG, IRDye 680RD conjugated antibody	LI-COR Biosciences	Cat#926-68076 RRID: AB_10956590
Goat polyclonal anti-rabbit antibody, HRP-conjugated	Dako	Cat# P0448; RRID:AB_2617138
Polyclonal goat anti-mouse IgG (H + L) Antibody, HRP-conjugated	Thermo Fisher Scientific	Cat# 31430; RRID:AB_228307
Anti-rat IgG, HRP-linked Antibody	Cell Signaling Technology	Cat# 7077S; RRID:AB_10694715
Goat anti-rabbit IgG (H + L) Cross-Adsorbed Secondary Antibody, Alexa Fluor™ 405	Thermo Fisher Scientific	Cat# A-31556; RRID:AB_221605

(Continued on next page)

Continued

REAGENT or RESOURCE	SOURCE	IDENTIFIER
Bacterial and virus strains		
BL21(DE3) Competent E. coli	NEB	Cat# C2527H
One Shot™Stb3™ Chemically Competent E. coli	Thermo Fisher Scientific	Cat# C737303
Biological samples		
Myc-overexpressed primary liver tumors	This study	N/A
Liver tissues	This study	N/A
Chemicals, peptides, and recombinant proteins		
GST alone	This study	N/A
GST-LC3A	This study	N/A
GST-LC3B	This study	N/A
GST-LC3C	This study	N/A
GST-GABARAP	This study	N/A
GST-GABARAP L1	This study	N/A
GST-GABARAP L2	This study	N/A
YTHDF2 aa 244-257-SKPAKQQPKLKTKN	This study, Peps4LS, Heidelberg, Germany	N/A
YTHDF2 aa 244-257 Biotin-SKPAKQQPKLKTKN	This study, Peps4LS, Heidelberg, Germany	N/A
CpG2006	TIB MOLBIOL, Berlin	N/A
incomplete Freund's adjuvant	Merck	F5506
13C15N-labeled C-terminal arginine DGLNDDDFEPYLS(phosphorylated)PQAR	This study (for SRM)	N/A
13C15N-labeled C-terminal arginine DGLNDDDFEPYLSQPQAR	This study (for SRM)	N/A
EDTA-free protease inhibitor	Roche	Cat# 11873580001
[Ac]-YGLNDDDFEPYLSQA-[NH2]	This study (for ITC)	N/A
[Ac]-YGLNDDDFEPYLS(phosphorylated)PQA-[NH2]	This study (for ITC)	N/A
Matrigel	Corning	Cat#356230
Hygromycin B	Invitrogen	Cat#10687010
Hoechst 33342	Thermo Fisher Scientific	Cat#H1399
Coomassie Brilliant Blue R250	Biorad	Cat#1610436
EDC (1-ethyl-3-(3-dimethylaminopropyl) - carbodiimide hydrochloride	Sigma Aldrich	Cat#25952-53-8
Penicillin/Streptomycin	Sigma Aldrich	Cat#P0781
AEBSF	Sigma Aldrich	Cat#A8456
γ-32P-ATP	Hartmann Analytic	Cat#FP-501
Illustra MicroSpin G-25 columns	Cytiva	Cat#27532501
TRIzol Reagent	Zymo Research	Cat#R2050-1-200
Alkaline phosphatase	Sigma Aldrich	Cat#P0114
Phosphodiesterase I	Sigma Aldrich	Cat#P3243
Benzonase	Sigma Aldrich	Cat#E1014
Tetrahyrouridine	Sigma Aldrich	Cat#584222
Butylated hydroxytoluene	Sigma Aldrich	Cat#PHR111
Pentostatin	Sigma Aldrich	Cat#116860
Stable isotope-labeled internal standard (SILIS)	In-House (Kaiser lab)	N/A
Guanosin	Sigma Aldrich	Cat#BCCJ8525
N6-Methyladenosin	Biosynth	Cat#NM32281-1503
T4 polynucleotide kinase	Thermo Fisher Scientific	Cat#EK0031

(Continued on next page)

Continued

REAGENT or RESOURCE	SOURCE	IDENTIFIER
Critical commercial assays		
XTT colorimetric assay kit	Roche	Cat# 11465015001
Oligo d(T)25 Magnetic beads	NEB	S1419S
NucleoSpin RNA Kit	Macherey-Nagel	740955.50
Annexin V FITC-conjugated	Immunotools	Cat# 31490013
RevertAid First Strand cDNA Synthesis Kit	Thermo Fisher Scientific	Cat#K1622
Megaprime DNA-Labeling Systems kit		Cat# RPN1606
Takyon® No ROX SYBR 2X MasterMix blue dTTP	Eurogentec	Cat#UF-NSMT-B0701
Sso Fast Eva Green Mix	Bio-Rad	Cat# 1725202
Protein G Dynabeads	Invitrogen	Cat# 10003D
Protein G Sepharose beads	GE Healthcare/Sigma	Cat# GE17-0618-05
RNA Clean & Concentrator Kit	Zymo Research	Cat# R1014
Eukaryote RiboMinus Kit v2	Thermo Fisher Scientific	Cat# A15020
First-strand cDNA synthesis kit	Thermo Fisher Scientific	Cat#K1612
Phusion High-Fidelity DNA Polymerase	NEB	Cat#M0530L
MycStrip® - Mycoplasma Detection Kit	Invivogen	Cat#rep-mysnc-100
Experimental models: Cell lines		
myeloma cell line P3X63-Ag8.653	ATCC	Cat# CRL-1580
HEK293T	ATCC	Cat# CRL-3216
Hela	ATCC	Cat# CCL-2
MRC5	ATCC	Cat# CCL-171
hTERT RPE-1	ATCC	Cat# CRL-4000
NIH-3T3	ATCC	Cat# CRL-1658
Sw620	ATCC	Cat# CCL-227
A549 (ATCC)	Laura Manelyte, University of Regensburg, Germany	Cat# CCL-185
C643	Stefan Hüttelmaier, Martin Luther University Halle-Wittenberg, Germany	RRID:CVCL_5969
BJ-h-TERT	Anders Lund, BRIC, Copenhagen	N/A
HT-29	ATCC	HTB-38
HCT116 (DSMZ)	Martin Ehrenschrwender, University Hospital Regensburg, Germany	DSMZ no.: ACC 581
NRK (ATCC)	Joachim Wegener, University of Regensburg, Germany	Cat# CRL-6509
HCT116.Luc	This study	N/A
HCT116.Luc YTHDF2 ko clone 1	This study	N/A
HCT116.Luc YTHDF2 ko clone 2	This study	N/A
HCT116.Luc YTHDF2 ko clone 4	This study	N/A
HCT116.Luc YTHDF2 ko clone 5	This study	N/A
U2OS-GFP-LC3-RFP-LC3ΔG (pool)	This study	N/A
MRC5-GFP-LC3-RFP-LC3ΔG (pool)	This study	N/A
BJ-GFP-LC3-RFP-LC3ΔG (pool)	This study	N/A
HEK293T-GFP-LC3-RFP-LC3ΔG (single clone)	This study	N/A
RPE1-GFP-LC3-RFP-LC3ΔG (single clone)	Diehl et al. ⁴⁷	N/A
Experimental models: Organisms/strains		
Lou/c rats	Beckers and Bazin ⁴⁸	Lou/c
C57BL/6 mice	Charles River	C57BL/6J
NOD.Cg-Prkdc ^{scid} Il2rg ^{tm1Wjl} /SzJ	The Jackson Laboratory	RRID:IMSR_JAX:005557

(Continued on next page)

Continued

REAGENT or RESOURCE	SOURCE	IDENTIFIER
Oligonucleotides		
siPOOLS targeting YTHDF1	This study, siTOOLS Biotech	N/A
siPOOLS targeting YTHDF2	This study, siTOOLS Biotech	N/A
siPOOLS targeting YTHDF3	This study, siTOOLS Biotech	N/A
siPOOLS targeting KIF11	This study, siTOOLS Biotech	N/A
Control siRNA pool (siPOOLS)	This study, siTOOLS Biotech	N/A
RT-qPCR; Ki67 F: GAAAGAGTGGCAACCTGCCTTC	Metabion international and Integrated DNA Technologies (IDT)	N/A
RT-qPCR; Ki67 R: GCACCAAGTTTTACTACATCTGCC	Metabion international and Integrated DNA Technologies (IDT)	N/A
RT-qPCR; RPL32 F: AGGCATTGACAACAGGGTTC	Metabion international and Integrated DNA Technologies (IDT)	N/A
RT-qPCR; RPL32 R: GTTGACATCAGCAGCACTT	Metabion international and Integrated DNA Technologies (IDT)	N/A
RT-qPCR; YTHDF1 F: CAAGCACACAACCTCCATCTTCG	Metabion international and Integrated DNA Technologies (IDT)	N/A
RT-qPCR; YTHDF1 R: GTAAGAACTGGTTCGCCCTCAT	Metabion international and Integrated DNA Technologies (IDT)	N/A
RT-qPCR; YTHDF2 F: TAGCCAGCTACAAGCACACCAC	Metabion international and Integrated DNA Technologies (IDT)	N/A
RT-qPCR; YTHDF2 R: CAACCGTTGCTGCAGTCTGTGT	Metabion international and Integrated DNA Technologies (IDT)	N/A
RT-qPCR; YTHDF3 F: GCTACTTTCAAGCATACCACCTC	Metabion international and Integrated DNA Technologies (IDT)	N/A
RT-qPCR; YTHDF3 R: ACAGGACATCTTCATACGGTTATTG	Metabion international and Integrated DNA Technologies (IDT)	N/A
RT-qPCR; ALDOA F: GACACTCTACCAGAAGGCGGAT	Metabion international and Integrated DNA Technologies (IDT)	N/A
RT-qPCR; ALDOA R: GGTGGTAGTCTCGCCATTTGTC	Metabion international and Integrated DNA Technologies (IDT)	N/A
RT-qPCR; CDKN1B F: ATAAGGAAGCGACCTGCAACCG	Metabion international and Integrated DNA Technologies (IDT)	N/A
RT-qPCR; CDKN1B R: TTCTTGGGCGTCTGCTCCACAG	Metabion international and Integrated DNA Technologies (IDT)	N/A
Northern Blot; GAPDH: CATGGACTGTGGTCATG AGTCCTTCCACGATACCAAAGTT	Metabion international and Integrated DNA Technologies (IDT)	N/A
northern blot; GAPDH: GAATTTGCCATGGGTGGAATC ATATTGGAACATGTAACCATGTAGTTGAGG	Metabion international and Integrated DNA Technologies (IDT)	N/A
northern blot; GAPDH: TGTTGCTGTAGCCAAATTC GTTGTCATACCAGGAAATGAGCTT	Metabion international and Integrated DNA Technologies (IDT)	N/A
Northern blot; 7SK: ACTCGTATACCCTTGACCGAAGA	Metabion international and Integrated DNA Technologies (IDT)	N/A
Recombinant DNA		
pCW57-HygB- EGFP-YTHDF2-P2A-mCherry	This study	N/A
pMRX-IP-GFP-LC3-RFP-LC3ΔG	Kaizuka et al. ³²	Addgene plasmid #84572
pcDNA5-EGFP-NLS-P2A-mCherry-PTS1	Pan et al. ⁴⁹	Addgene plasmid #87803
pCW57-HygB-EGFP-YTHDF2-P2A-mCherry	This study	N/A
c-myc-PT3EF1a	Xin Chen	Addgene Plasmid #92046
PX330-sg-Tp53	Kuznetsov et al. ⁵⁰	N/A
SB100 transposase-encoding plasmids	Mark Groudine	Addgene Plasmid #127909
pCW57-MCS1-P2A-MCS2 (Hygro)	Adam Karpf	Addgene plasmid #80922
pLARTA _{lacZ}	Markus Kretz	N/A

(Continued on next page)

Continued

REAGENT or RESOURCE	SOURCE	IDENTIFIER
pGL3 Basic Vector	Promega	Cat#E1751
pLARTA-Luciferase	This study	N/A
px459 v2.0-YTHDF2 gRNA1	This study	N/A
pIRES-Neo-Flag/HA-N terminal empty	Meister lab	N/A
pIRES-Neo-Flag/HA-C terminal empty	Meister lab	N/A
pIRES-Neo-Flag/HA-YTHDF2	This study	N/A
pIRES-Neo-Flag/HA-YTHDF2-(1–385)	This study	N/A
pIRES-Neo-Flag/HA-YTHDF2-(386–579)	This study	N/A
pIRES-Neo-Flag/HA-YTHDF2-5A mut	This study	N/A
pCS2-6xMyc-empty	This study	N/A
pCS2-6xMyc-LC3A	This study	N/A
pCS2-6xMyc-LC3B	This study	N/A
pCS2-6xMyc-LC3C	This study	N/A
pCS2-6xMyc-GABARAP	This study	N/A
pCS2-6xMyc-GABARAP L1	This study	N/A
pCS2-6xMyc-GABARAP L2	This study	N/A
pIRES-Neo-EGFP-YTHDF2-Flag/HA-C terminal	This study	N/A
pIRES-Neo-EGFP-YTHDF2-(1–385)-Flag/HA-C terminal	This study	N/A
pIRES-Neo-EGFP-YTHDF2-(1–385)-4xLIR mut-Flag/HA-C terminal	This study	N/A
pIRES-Neo-EGFP-YTHDF2-(385–579)-Flag/HA-C terminal	This study	N/A
pIRES-Neo-EGFP-YTHDF2-(385–579)-LIR8 mut-Flag/HA-C terminal	This study	N/A
Software and algorithms		
FlowJo version 10	N/A	N/A
Skyline	MacCoss Lab Software	N/A
OrthoDB v12	Kuznetsov et al. ⁵⁰	N/A
Muscle	Edgar. ⁵¹	N/A
Jalview	https://jalview.org	N/A
Jensen-Shannon divergence approach	Capra and Singh. ⁵²	N/A
iLIR prediction tools	Kalvari et al. ³⁴	N/A
AlphaFold2.3 Multimer (AF2)	Jumper et al., ⁵³ https://doi.org/10.1101/2021.10.04.46303457 , Stuke and Hummer. ⁵⁴	N/A
AlphaFold3 (AF3)	Abramson et al. ⁵⁵	N/A
UniProt	https://uniprot.org	UniProtKB (RRID:SCR_004426)
charmm36m (July 2021 version)	Huang et al. ⁵⁶	N/A
Gromacs (versions 2023.2 and 2023.3)	https://doi.org/10.1016/j.softx.2015.06.001	N/A
Python 3 with the MD Analysis	Michaud-Agrawal et al. ⁵⁷	N/A
VMD	Humphrey et al. ⁵⁸	N/A
Odyssey	LI-COR Biosciences	Odyssey CLx, RRID: SCR_014579
NITPIC	Keller et al. ⁵⁹	N/A
SEDPHAT	Houtman et al. ⁶⁰	N/A
GUSSI	Brautigam et al. ⁶¹	N/A

(Continued on next page)

Continued

REAGENT or RESOURCE	SOURCE	IDENTIFIER
Other		
Amersham Hybond-N+ membrane	Cytiva	Cat# RPN303B
Acclaim Pepmap100 C18 nano column, 75 μ m i.d.x150 mm	Thermo Fisher Scientific	N/A
Acclaim Pepmap100 pre-concentration column 100 μ m i.d.x20mm	Thermo Fisher Scientific	N/A
Personal Molecular Imager System	Biorad	N/A
Incucyte® S3 Live-Cell Analysis System	Satorius	Cat#4647
Incucyte® SX5 Live-Cell Analysis System	Satorius	Cat#4816
CFX96real-Time System BioRad	Biorad	N/A
Echo® 550 Liquid Handler	Beckman Coulter	N/A
Multidrop™ Combi Reagent Dispenser	Thermo Fisher Scientific	Cat#5840330
HandyStep® touch	Brandt	Cat# 705211
NuPAGE 4–12% Bis-Tris protein gels	Invitrogene	Cat#NP0321PK2

EXPERIMENTAL MODEL AND STUDY PARTICIPANT DETAILS

Cell lines

HEK293T (ATCC), HeLa (ATCC), MRC5 (ATCC), hTERT RPE-1 (ATCC, referred to as RPE-1), NIH-3T3 (ATCC), Sw620 (ATCC), A549 (ATCC), C643 (CLS, RRID:CVCL_5969), BJ-hTERT cells were cultivated in Dulbecco's modified Eagle's medium (DMEM) supplemented with 10% fetal bovine serum (FBS) and 1% Penicillin/Streptomycin (P/S) antibiotics mix (all from Sigma-Aldrich, St. Louis, Missouri, USA). A549 cells were a gift from Laura Manelyte, University of Regensburg, Germany. BJ-hTERT, now referred to as BJ, cells were a gift from Anders Lund, BRIC, University of Copenhagen, Denmark.

HCT116 (DSMZ, Braunschweig, Germany) and HT-29 (ATCC) cells were cultivated in McCoy's 5A (Modified) medium (Gibco) supplemented with 10% fetal bovine serum (Sigma-Aldrich, St. Louis, Missouri, USA) and 1% Penicillin/Streptomycin (P/S) antibiotics mix. HCT116 cells were a gift from Martin Ehrenschröder, University Hospital Regensburg, Germany.

Normal rat kidney (NRK, DSMZ, Braunschweig, Germany) cells were cultured in DMEM including 4.5 g/L D-glucose, 2 mM L-glutamine, 100 μ g/mL Penicillin/Streptomycin (P/S) and 5% (v/v) fetal calf serum. NRK cells were a gift from Joachim Wegener, University of Regensburg, Germany.

Most cell lines used in this study were either obtained directly from ATCC or DSMZ, and thus came pre-authenticated by the respective providers. Cell lines obtained from the mentioned laboratories were authenticated using short tandem repeat (STR) profiling. Furthermore, all cell lines were routinely tested for mycoplasma contamination using PCR-based assays or commercially available detection kits (MycosStrip – Mycoplasma Detection Kit, Cat# rep-mysnc-100, InvivoGen). Only mycoplasma-free cell lines were used in experiments.

Animal models for the development of monoclonal antibodies against YTHDF2

Lou/c rats and C57BL/6 mice were used for the development of monoclonal antibodies against YTHDF2 (see detailed method below). Animal procedures were conducted in accordance with the German Animal Welfare Law and with approval by the local authorities of Upper Bavaria, Germany (reference number Az. 55.2-1-54-2532.6-4-99). Sex and gender were not considered in this study, and potential differences were not assessed.

In vivo experiments for myc-related experiments

Animals were performed in accordance with European, national, and institutional guidelines. The protocols were approved by the Regierungspräsidium Darmstadt of the state of Hessen, Germany (FU/2012). C57BL/6 mice were obtained from Jackson Laboratories and were housed in standard cages in pathogen-free facilities on a 12-h light/dark cycle with *ad libitum* access to food and water. DNA plasmids used for *in vivo* experiments were produced using the plasmid PlusMega kit (QIAGEN, Cat. No. 12941). Experimental animals were monitored at least bi-weekly, and tumor growth was followed by MRT. Once the animals were sacrificed, normal liver and tumor tissue were collected and frozen. Later protein was extracted and protein lysates subjected to immunoblotting. Sex and gender were not considered in this study, and potential differences were not assessed.

Hydrodynamic tail-vein injection

Hydrodynamic tail vein injection was performed as described previously.⁶² Animals were closely examined before the experiments to ensure their health status. Female mice (6–8 weeks old) were injected with a sterile mix of 0.9% NaCl solution/plasmid

corresponding to 10% of their body weight. Each mouse received 12 μ g of c-myc-PT3EF1a, 12 μ g of PX330-sg-Tp53,⁶² and 2 μ g of SB100 transposase-encoding plasmids (SB100X). c-myc-PT3EF1a was a gift from Xin Chen, Department of Bioengineering and Therapeutic Sciences and Liver Center, University of California, San Francisco, CA. SB100X was a gift from Mark Groudine (ref.: Addgene plasmid # 127909; <http://n2t.net/addgene:127909>; RRID:Addgene_127909). Mice were injected into lateral tail veins in 5–8 s to develop tumors. Hydrodynamic tail injection was performed under isofluorane anesthesia. Vectors for hydrodynamic delivery were produced using the plasmid PlusMega kit (QIAGEN, Cat. No. 12941) following the manufacturer's instructions.

Xenograft

Mouse experiments were conducted in accordance with institutional guidelines of the Institute of Molecular Genetics, Czech Academy of Science, and approved under the project license PP63-2018. Thirteen- to fifteen-week-old, male, immuno-deficient mice (NOD.Cg-Prkdc^{scid} Il2rg^{tm1Wjl}/SzJ) were purchased from The Jackson Laboratory and housed under specific-pathogen-free conditions with daily 12 h light and 12 h dark cycles. Tumors were generated by subcutaneous injection of 0.5×10^6 HCT116 and YTHDF2-KO cells in a 1:1 dilution of PBS:Matrigel (Corning Matrigel, #356230) into the flanks of immunodeficient mice using a 26G needle ($n \geq 7$ per group). Tumor growth was regularly monitored by caliper measurement week after injection to determine tumor size and animal welfare. Sex and gender were not considered in this study, and potential differences were not assessed.

Human participants

No human participants were involved in this study.

METHOD DETAILS

Plasmids, antibodies and siPOOLS

Flag/HA tagged YTHDF2 was cloned into pIRES-Neo plasmids. YTHDF2 was cloned into pcDNA5-EGFP-NLS-P2A-mCherry-PTS1 (Addgene plasmid #87803)⁴⁹ by replacing the NLS sequence with YTHDF2 sequence. pcDNA5-EGFP-NLS-P2A-mCherry-PTS1 was a gift from Andrea Musacchio. Subsequently, EGFP-YTHDF2-P2A-mCherry was cloned into the lentiviral vector pCW57-MCS1-P2A-MCS2 (Hygro) (Addgene plasmid #80922) to have pCW57-HygB-EGFP-YTHDF2-P2A-mCherry. pCW57-MCS1-P2A-MCS2 (Hygro) was a gift from Adam Karpf. c-myc-PT3EF1a (Plasmid #92046) c-myc-PT3EF1a was a gift from Xin Chen and was obtained from Addgene. pLARTA_{lacZ} was used as backbone to clone the pLARTA-Luciferase. pLARTA_{lacZ} was a gift from Markus Kretz. Luciferase was obtained from pGL3 Basic Vector (Promega).

The following antibodies were used for western blots: anti-YTHDF1 (rabbit polyclonal, 17479-1-AP, 1:1000, ProteinTech), anti-YTHDF2 (rat monoclonal, clone 9G11), anti-YTHDF2 (mouse monoclonal, clone 32A11), anti-YTHDF2 (rabbit polyclonal, 1:1000, 24744-1-AP, 1:1000, ProteinTech), anti-YTHDF3 (mouse monoclonal, 1:500, sc-377119, Santa Cruz Biotechnology), anti-YTHDF3 (rabbit polyclonal, 1:1000, 24744-1-AP, 1:1000, ProteinTech), anti-beta-Tubulin (rabbit polyclonal, 1:1000, Abcam, ab6046), anti-GAPDH (mouse monoclonal, 1:1000, GeneTex, GTX627408), anti-p27 (rabbit monoclonal, 1:1000, Cell Signaling Technology, 3686S), anti-LC3A/B (rabbit polyclonal, 1:1000, Cell Signaling Technology, 4108S), Anti-LC3 pAb (rabbit polyclonal, 1:1000, MBL Life Sciences, PM036) anti-CDK6 (mouse monoclonal, 1:100, Santa Cruz Biotechnology, sc-7961), anti-HA tag (Rabbit mAb, Cell Signaling, 3724T), anti-c-Myc (Rabbit mAb, Cell Signaling, 5605S), anti-Myc-tag (71D10) (Rabbit mAb, Cell Signaling, 2278), anti-Phospho-p70 S6 Kinase (Thr421/Ser424) (Rabbit polyclonal, 1:1000, Cell Signaling, 9204S), anti-Phospho-p70 S6 Kinase (Thr389) (Rabbit polyclonal, 1:1000, Cell Signaling, 9205S), anti-p70 S6 Kinase Antibody (Rabbit polyclonal, 1:1000, Cell Signaling, 9202S). Goat-*anti*-mouse/rat/rabbit IRDye 680RD or goat-*anti*-mouse/rat/rabbit IRDye 800CW antibodies (Li-Cor Biosciences, Lincoln, NE, USA) were used as secondary antibodies.

siPOOLS targeting YTHDF1, 2, 3 were purchased from siTOOLS Biotech (Planegg/Martinsried, Germany).

Generation of a monoclonal antibody against YTHDF2

A peptide representing YTHDF2 (aa 244-257-SKPAKQQPKLTKN) was synthesized and coupled to ovalbumin or biotin (Peps4LS, Heidelberg, Germany). Lou/c rats and C57BL/6 mice were immunized subcutaneously (s.c.) and intraperitoneally (i.p.) with a mixture of 50 μ g OVA-coupled peptides in 500 μ L PBS, 5 nmol CpG2006 (TIB MOLBIOL, Berlin, Germany), and 500 μ L incomplete Freund's adjuvant. After 6 weeks, a boost without Freund's adjuvant was given i.p. and s.c. 3 days before fusion. Fusion of the myeloma cell line P3X63-Ag8.653 with the immune spleen cells was performed according to standard procedure. After fusion, the cells were plated in 96-well plates using RPMI 1640 with 20% fetal calf serum, glutamine, pyruvate, non-essential amino acids and HAT media supplement (Hybri-Max, Sigma-Aldrich). Hybridoma supernatants were screened 10 days later by ELISA on biotinylated peptides and binding was detected using HRP-labelled isotype-specific monoclonal mouse-*anti*-rat IgG or rat-*anti*-mouse secondary antibodies. Positive supernatants were further validated by Western blot analysis and hybridoma cells were subcloned by limiting dilution to obtain stable monoclonal cell lines. Experiments in this work were performed with hybridoma supernatant YTHDF2 9G11 (rat IgG2a) and YTHDF2 32A11 (mouse IgG1).

Cell culture and generation of stable cell lines

Lentiviral particles were produced in HEK293T cells using pCW57-HygB-EGFP-YTHDF2-P2A-mCherry and pMD2.G and psPAX2. RPE1 and MRC5 cells were transduced with lentivirus for expressing YTHDF2. Retroviral particles were produced in HEK293T using pMRX-IP-GFP-LC3-RFP-LC3ΔG (Addgene plasmid #84572) plasmids, packaging plasmid (pCMV-Gag-Pol) and the envelope plasmid (pCMV-VSV-G). pMRX-IP-GFP-LC3-RFP-LC3ΔG (Addgene plasmid #84572) was a gift from Noboru Mizushima (University of Tokyo, Tokyo, Japan). The U2OS, MRC5, BJ, HEK293T cells were transduced with retrovirus for autophagy reporter. Single clone RPE1 expressing GFP-LC3-RFP-LC3ΔG was used as described previously.⁴⁷ Briefly, the cells were plated and propagated in 6-well plates overnight. On the next day, transduction with viruses was performed. Two days later, transduced cells with pCW57-HygB-EGFP-YTHDF2-P2A-mCherry plasmids were selected using 100 μg/mL Hygromycin B while cells transduced with pMRX-IP-GFP-LC3-RFP-LC3ΔG were selected with 2 μg/mL puromycin (Invitrogen, Thermo Fisher Scientific, Waltham, Massachusetts, USA) for at least 3 passages.

HCT116.Luc was generated by lentiviral transfection of the HCT116 wt cells with pLARTA-Luc followed by antibiotics selection using G418 (300 μg/mL). Knockout cells for YTHDF2 were created using the CRISPR/Cas9 genome editing. Briefly, HCT116.Luc cells were transfected with px459 v2.0-YTHDF2 gRNA1 (GTCCATTACTAGTAACATCG) using Lipofectamine 2000, according to the manufacturer's instructions. After selection with puromycin, single clones were seeded in a 96-well plate and then expanded to a 6-well plate. Knockout clones were tested by western blotting using a specific antibody against YTHDF2 (clone 9G11).

Autophagy inhibition was performed using 300 nM final concentrations of Bafilomycin A1 (BML-CM110-0100, Enzo Life Sciences, Lörrach, Germany) or 10 μM final concentration Chloroquine (C6628-25G, Sigma-Aldrich, St. Louis, Missouri, USA) for 4 h 10 μM final concentration of MG-132 (Sigma-Aldrich, St. Louis, Missouri, USA) was used to inhibit proteasome. For 4 h 10 μg/mL final concentration of Brefeldin A (Sigma-Aldrich, St. Louis, Missouri, USA) was used for 4 h. As a control for all treatments, the same volume of vehicle (DMSO) was used.

Generation of protein lysates and western blot analyses

Lysates from mammalian cells: cells at 30% confluency were collected as low-density conditions. For the high-density condition, cells were seeded at 100% confluency and harvested 2 days later. Cells from both conditions were collected by cell scraper and lysed using NP-40 buffer.

In all analyses, lysates were cleared for 15 min, full speed, 4°C, and the protein concentration was determined via Bradford assay.

For performing a western blot, samples were mixed with 5× Laemmli Sample Buffer and separated on a 10–15% polyacrylamide gel. After separation, the proteins were blotted onto an Amersham Protran Premium 0.45 μm membrane (GE Healthcare, Chicago, IL, USA) using 1× Towbin buffer for 1 min/kDa constant at 2 mA/cm² using a semi-dry chamber (Trans-Blot SD Semi-Dry Transfer Cell, Bio-Rad). The membrane was blocked in TBS containing 0.1% Tween 20 and 5% milk. After incubation with suitable antibodies, the membrane was scanned on an LI-COR reader (Li-Cor Biosciences, Lincoln, NE, USA).

Co-immunoprecipitation (Co-IP)

For the co-IP experiment, HEK293T cells were transiently co-transfected with two constructs carrying either Flag/HA tagged YTHDF2 and Myc-tagged YFP/LC3/GABARAP for 48 h. Afterward, cells were washed with 1× PBS and lysed in ice-cold IP lysis buffer: 25 mM Tris-HCl, (pH 8.0), 1 mM EDTA, 1% (v/v) Triton X-100, 5% glycerol, 150 mM NaCl, cOmplete protease inhibitor cocktail (Roche), phosphatase inhibitor cocktail 2 and 3 (Sigma-Aldrich) and RNAase A. Samples were incubated on ice for 15 min and centrifuged at 20,000 × g for 15 min at 4°C. anti-HA beads (Sigma-Aldrich) were equilibrated and washed three times in 1 mL of ice-cold IP lysis buffer and were spun down at 1000 × g for 2 min at 4°C. In total, 1 mg of lysates was added to 5 μL of equilibrated anti-HA beads and incubated overnight at 4°C with constant mixing. Tubes were spun at 1000 × g for 3 min at 4°C. anti-HA beads were washed three times with 1 mL ice-cold wash buffer (25 mM Tris-HCl, (pH 8.0), 1 mM EDTA, 0.1% (v/v) Triton X-100, 5% glycerol, 300 mM NaCl). Fifteen μL of 1X SDS sample buffer was then added to the anti-HA beads and were boiled for 10 min at 95°C. Beads were collected by centrifugation at 2500 × g for 2 min and SDS-PAGE was performed with the supernatant.

Proliferation assay

Single cell suspensions were obtained after trypsinization and passing through a cell strainer. XTT was performed in 96 well plates using XTT colorimetric assay kit (11465015001, Roche, Switzerland) based on manufacturers' instruction. For assaying the knock-down condition using siPOOLS, the siRNA/Lipofectamine RNAiMAX/OptiMEM complexes were first seeded into the well in triplicate. Then the cells (1000 cells/well) for HCT116 cell lines were seeded into a 96-well plate and were assayed every day for five days.

The proliferation assay was performed in a 384-well plate using HCT116, MRC5, and RPE1 cell lines and monitored with Incucyte. A mastermix of 10 μL OptiMEM and 0.2 μL RNAiMAX per well was prepared, and 10 μL of this mix was dispensed into each well using the BRAND HandyStep Touch. Next, 15 nL of siRNA (10 μM stock, final concentration 3 nM) was added directly to the plate using the Echo 550 Liquid Handler. The plate was then briefly shaken with a Multidrop Dispenser and incubated at room temperature for 10–15 min. Subsequently, 40 μL of cell suspension at the desired concentration was added using the Multidrop Dispenser. Finally, the plate was placed in the Incucyte for live-cell imaging every 2 h for at least 5 days.

Cell cycle analysis

For assaying the knockdown condition using siPOOLS, the siRNA/Lipofectamine RNAiMAX/OptiMEM complexes were first seeded into the well and then the same amount of HCT116 cells (300,000 cells per well) were added to the well in 6-wells plate. The cell cycle analysis was performed two days post-transfection.

The cells were spun down at 100g and then washed with 1 × PBS at RT. The supernatant was removed and resuspended in 1 mL 70% cold methanol to fix and permeabilize the cells. After incubation overnight in a turning wheel in the cold room, the cells were washed two times with cold PBS, centrifuging each time at 800g for 5 min. After that, the cells were incubated for 30 min at 37°C in 1 mL PBS containing 1 mg/mL RNase A. The cells were then collected by centrifuging 5 min at 800g and resuspended in 500 mL DAPI solution (10 μL DAPI (1 mg/mL) in 10 mL in PBS containing 0.1% Triton X-100). The cell cycle was performed on the BD FACSCanto II and the data was analyzed by ModFit LT software.

Apoptosis analysis

Three days after knockdown of YTHDF proteins by siPOOLS in 6-wells plate, the medium in the culture vessel was collected and transferred to a 50 mL Falcon tube. The cells were then washed once with PBS and the PBS was also transferred into the 50 mL Falcon. After trypsinization, the cell suspension was also collected into the 50 mL Falcon. The 50 mL Falcon tube was centrifuged at 300g, 3 min, at 4°C. The cell pellet was resuspended in 70 μL 1 × binding buffer (10 mM HEPES, 140 mM NaCl, 2.5 mM CaCl₂, pH 7.4) containing 5 μL annexin V FITC (Immunotools, Cat-No. 31490013). After incubation for 20 min on ice in the dark, 10 μL DAPI (5 μg/mL) was added to the sample and data was collected using BD FACSCanto II.

Ribosome immunoprecipitation followed by qPCR (Ribo-IP-qPCR)

Human MRC5 cells were seeded with 1.5×10^3 cells/200 μL/cm² and 12.5×10^3 cells/200 μL/cm² into T150 dishes to get a confluency of 15% (Low density) and 125% (High density), respectively. After cultivation of two days under a humidified atmosphere of 95% air and 5% CO₂ at 37°C the low (30% confluency) and high density (300% confluency) cells were washed with PBS and harvested using a plastic scraper. Approximately 4×10^6 MRC5 were lysed using 400 μL buffer A (25 mM Tris-HCl pH 7.5, 150 mM NaCl, 15 mM MgCl₂, 1 mM DTT, 8% glycerol, 1% Triton X-100, 0.5% sodium deoxycholate, 100 μg/mL Cycloheximide (CHX), 100 U/mL RiboLock RNase Inhibitor, 25 U/mL DNase I, 1 mM AEBSF in nuclease-free water). The cell lysate was consecutively centrifuged twice at 800 g (5 min, 4°C), once at 8000 g (5 min, 4°C) and finally once at 20000 g (5 min, 4°C) to remove nuclei. To proceed with normalized amounts of LD and HD cell extract, RNA concentrations were measured using Nanodrop UV spectrophotometer. Immunoprecipitations (IPs) were performed with 3 μg rabbit anti-RPS3 (#11990-1-AP, Proteintech) and 3 μg goat anti-rabbit (#A-11012, Invitrogen) on typically 4 mg protein lysate from LD and HD cells. After overnight incubation with antibodies at 4°C, Protein G Dynabeads (Invitrogen), pre-blocked with BSA (1 mg/mL) were incubated with the samples for 4 h at 4°C. 30% sample in each IP was withdrawn to serve as an input for qPCR. Beads with bound ribosomes and their associated RNAs were washed three times with buffer C (25 mM Tris-HCl pH 7.5, 300 mM NaCl, 15 mM MgCl₂, 1 mM DTT, 1% Triton X-100, 0.5% sodium deoxycholate, 100 μg/mL CHX, 100 U/mL RiboLock RNase Inhibitor, 25 U/mL DNase I, 1 mM AEBSF in nuclease-free water) for 5 min each on a rotating wheel. RNA (enriched for actively translated RNA) was isolated from beads with TRIzol Reagent (#15596018, Ambion) and purified RNA (1.5 μg) was reverse transcribed to cDNA using RevertAid First Strand cDNA Synthesis Kit with random hexamer primers (#K1622, Thermo Scientific) according to the manufacturer's instructions. Resulting Ribo-IP cDNA and inputs on LD and HD cells were used as template for qPCR with Takyon No ROX SYBR 2X MasterMix blue dTTP (#UF-NSMT-B0701, Eurogentec) on a CFX96 Real-Time System (BioRad). To quantify cDNA targets the gene-specific primer pairs listed in the key resources table below were used. The delta-delta Ct method (ΔΔCt), taking primer efficiency into account, was used to normalize mRNA levels relative to RPL32.

RNA preparation, qPCR, and northern blot analysis

For the data in Figure 5 A-B, RNA extraction from mammalian cells was performed using the NucleoSpin RNA Kit (Macherey-Nagel, Düren, Germany) following the manufacturer's protocol. mRNA (poly(A)+ RNA) was isolated using Oligo d(T)25 Magnetic beads (NEB) according to the manufacturer's protocol. The flow-through was collected and served as poly(A)- RNA. The RNA after isolation was collected and cleaned up from the magnetic beads using the NucleoSpin RNA Kit (Macherey-Nagel).

qPCR was done with Sso Fast Eva Green Mix (Bio-Rad, Hercules, CA, USA) using 0.5 μM forward and 0.5 μM reverse primer and cDNA from 10 ng RNA as template. qPCR was run on a CFX96 cyclor (Bio-Rad) using the standard program given in the Sso-Fast EvaGreen SuperMix manual. Data were evaluated using the delta-delta Ct method (ΔΔCt) method with RPL32 as reference mRNA for normalization. The oligos for qPCR are listed in the [key resources table](#) below. GAPDH northern blot probes (a mix of three antisense oligos) and 7SK northern blot probes are listed in the [key resources table](#) below.

For northern blot, RNA was separated on a 1% MOPS/Agarose gel. The detailed northern blotting protocol for MOPS/Agarose gel was described earlier.⁶³ Briefly, after transferring the RNA onto the Amersham Hybond-N membrane (GE Healthcare) via capillary blotting, the RNA was UV-crosslinked to the membrane at 254 nm. The short DNA probes were labeled with 20 μCi of γ-³²P-ATP (Hartmann Analytics, Braunschweig, Germany) using T4 PNK enzyme (Life Technologies) while the cDNA probes were prepared using Megaprime DNA-Labeling Systems kit (Cytiva, Global Life Sciences Solutions, Marlborough, MA, USA). The probes were purified using Illustra MicroSpin G-25 columns (GE Healthcare), and flow-through was collected and used for hybridization in the hybridization solution (5 × SSC, 20 mM NaPi pH 7.2, 7% SDS, 0.02% Albumin fraction V, 0.02% Ficoll 400, 0.02% polyvinylpyrrolidone K30).

After washing the membrane with suitable buffers, the membrane was exposed to a phosphor screen, and then signals were scanned by Personal Molecular Imager System (Bio-Rad).

Autophagy flux assay

For autophagy flux assay, the detailed protocol was described earlier.³³ Briefly, cells were seeded at desired concentration a day before. Fluorescence of GFP and RFP, as well as cell confluence (phase), were monitored over time via the IncuCyte S3 (Sartorius, Germany) in 384-well format. The first scan was executed 16 h after cell seeding. Screens in all three channels were taken at indicated time points following the treatment. Autophagy flux was monitored through changes in the ratio of the total fluorescence intensity of RFP/GFP. Each point represents the average ratio of data obtained from three individual wells (technical replicates).

Immunofluorescence

For immunofluorescence staining, HCT116 cells expressing EGFP-YTHDF2 cells were induced with Doxycycline (1 μ g/mL final concentration) 16 h before. Cells were then washed once with PBS and fixed with 4% paraformaldehyde in PBS for 10 min at 37°C. Fixation was stopped by PBS + 100 mM glycine for 5 min at room temperature. Cells were then washed twice with PBS and mounted using Prolong Gold + DAPI (Life Technologies). Confocal microscopy was carried out on a Zeiss LSM 780 microscope.

Analysis of publicly available human datasets

Kaplan-Meier curves for liver cancer patient survival curves were estimated with the online tool KM plotter⁶⁴ based on GEO, EGA and TCGA datasets. Using the KM plotter online tool, patients were split using the option 'Auto select best cutoff' in high or low YTHDF gene expression groups. Log Rank *p*-values were automatically calculated by the online tool KM plotter.

Graphic comparing gene expression between normal and tumor human samples were generated using the online tool GEPIA.²⁷ For GEPIA, the differential analysis was based on TCGA tumors versus (TCGA normal, whereas the expression data was log2 (TPM+1) - transformed and the log2FC was defined as median (tumor) - median (normal). *p*-values were calculated with a one-way ANOVA comparing tumor with normal samples. Correlation analysis was calculated using GEPIA software. The analysis was based on the expression of the dataset "TCGA tumors", The gene-sets and number of samples indicated in figure legends were used for correlation analysis.

Boxplots comparing relative protein abundance (TMT log2 ratio) between normal and tumor samples were generated using the online tool Cancer Proteogenomic Data Analysis Site (website: cProSite - Cancer Proteogenomic Data Analysis Site <https://cprosite.ccr.cancer.gov/>.) based on National Cancer Institute's Clinical Proteomic Tumor Analysis Consortium (CPTAC) and National Cancer Institute's International Cancer Proteogenome Consortium (ICPC) datasets.

Boxplots comparing relative gene expression abundance between normal, tumor and metastatic samples were generated using the online tool tnmplot.com.⁶⁵ The online tool tnmplot.com based their analysis on data generated by either gene arrays from the Gene Expression Omnibus of the National Center for Biotechnology Information (NCBI-GEO) or RNA-seq from The Cancer Genome Atlas (TCGA), Therapeutically Applicable Research to Generate Effective Treatments (TARGET), and The Genotype-Tissue Expression (GTEx) repositories.⁶⁵ The *p*-values were calculated automatically by the online tool using Kruskal-Wallis test.

ROC curves with AUC calculations were generated using the online tool rocplot.com.⁶⁶ The patients were divided in two cohorts (responder and non-responder to chemotherapies) based on their clinical characteristics (RECIST criteria for colon cancer patients; Relapse free survival at 6 months for ovarian cancer patients). The two cohorts were automatically compared using Mann-Whitney test or Receiver Operating Characteristic test in the R statistical environment (www.r-project.org) using Bioconductor libraries (www.bioconductor.org) by the online tool.

Autophagosome isolation

Autophagosome isolation was performed using a protocol published previously.³⁸ Cells were collected using Trypsin/EDTA, centrifuged with 1000 rpm for 5 min, and resuspended in PBS supplemented with EDTA-free protease inhibitor (Roche, ref. 11873580001). Cell disruption was performed using a Sonopuls Bandelin ultrasonic processor for 3 \times 2 sec with an amplitude of 60%. Lysates were centrifuged with 3,000g for 10 min at 4°C. Supernatants were centrifuged at 150,000g for 30 min at 4°C using Beckman coulter Optima MAX-XP Ultracentrifuge. Pellets were resuspended in PBS and 4 μ g of primary antibody GABRAP (Abcam, ab109364) was added for 30 min, followed by 12 μ g of 405-conjugated secondary antibody for 2h (Invitrogen, A31556) at 4°C. The samples were then centrifuged with 150,000g for 30 min at 4°C, and pellets were resuspended in PBS EDTA-free protease inhibitor solution. Autophagic vesicle sorting was performed using SONY Cell Sorter (SH800S) equipped with a 70 μ m chip. The vesicles were defined as AF-405-positive events, based on the background given by a secondary only negative control. A second discrimination plot was defined based on AF-488 positive events within the AF-405 population. Autophagic vesicles were sorted at minimum speed (flow rate 2). Afterward, TRIzol was added to the samples to perform RNA isolation. The gating of FACS data was performed using FlowJo version 10.

Total RNA isolation

Total RNA was extracted from autophagosomes under various experimental conditions (low/high cell density, presence/absence of GFP-tagged YTHDF2 proteins, and with/without Torin-1 treatment) using 500 μ L of TRIzol reagent, in accordance with the manufacturer's protocol (Zymo Research, California, USA). RNA isolation was carried out by adding 100 μ L of chloroform, followed by phase

separation and precipitation with cold isopropanol. After overnight incubation, the samples were centrifuged at $12,000 \times g$ for 60 min at 4°C . The supernatant was removed, and the RNA was washed twice with 200 μL of ethanol 70%. Remaining ethanol was removed after a 10-min air-drying step, and the RNA pellet was suspended in 15 μL of nuclease-free water.

mRNA enrichment

Small RNAs (<200 nts) were removed using the RNA Clean & Concentrator Kit (Zymo Research, Irvine, CA, USA) with 0.5–2 μg of total RNA as input material. The purified RNA fraction containing large RNAs (>200 nts) was resuspended in 10 μL of H_2O and subsequently subjected to ribosomal RNA (rRNA) depletion using the Eukaryote RiboMinus Kit v2 (Thermo Fisher, Waltham, MA, USA). Following rRNA removal and ethanol precipitation, the purified mRNA was resuspended in 12 μL of water. The absence of transfer RNAs and ribosomal RNAs was assessed using an Agilent 2100 Bioanalyzer pico assay.

RNA digestion

20–250 ng of total RNA and 5–15 ng enriched mRNA of each sample were hydrolyzed to single nucleosides in a volume of 17.5 μL by using 0.8 U alkaline phosphatase, 0.08 U phosphodiesterase I and 0.8 U benzonase in Tris (pH 8, 5 mM) and MgCl_2 (1 mM) containing buffer. Furthermore, 2 μg tetrahydouridine, 4 μM butylated hydroxytoluene and 0.4 μg pentostatin were added to avoid deamination and oxidation of the nucleosides. After incubation for 2 h at 37°C , 7.5 μL of LC-MS buffer (5 mM NH_4OAc , brought to pH 5.3 with glacial acetic acid) was added. For LC-MS/MS analysis, 15 μL of each sample was injected and 1 μL stable isotope-labeled internal standard (SILIS) was spiked into.

Nucleoside mass spectrometry

For quantitative mass spectrometry, an Agilent 1290 Infinity II combined with an Agilent Technologies G6470A QQQ system and electrospray ionization was used. For separation of Nucleosides a Fusion-RP column at 35°C and a flow rate of 0.35 mL/min was used. Buffer A was LC-MS buffer, eluent B was Ultra LC-MS grade acetonitrile. The gradient started at 100% solvent A for 1 min, followed by an increase to 10% solvent B over 4 min. From 5 to 7 min, solvent B was increased to 40% and maintained for 1 min before returning to 100% solvent A in 0.5 min and a 2.5 min re-equilibration period. The instrument was operated in dynamic MRM mode.

Quantification of nucleosides

For calibration, synthetic nucleosides were weighed and dissolved in water to a stock concentration of 1–10 mM. The calibration solutions ranged from 0.025 to 100 pmol for each canonical nucleoside and from 0.00125 pmol to 5 pmol for each modified nucleoside. Each calibration was spiked with 1 μL SILIS. Data were analyzed by the quantitative and qualitative MassHunter Software from Agilent. $m^6\text{A}$ levels were normalized to 1000 Guanosin to avoid biases based on different injected RNA amounts.

Immunoprecipitation (IP) of endogenous YTHDF2

For IP experiment, monoclonal antibodies for human YTHDF2 (clone 9G11) were coupled to 50 μL Protein G Sepharose beads overnight at 4°C . Antibody-decorated beads were washed twice with lysis buffer [25 mM Tris-HCl pH 7.4, 150 mM KCl, 0.5% (v/v) NP-40, 2 mM EDTA, 1 mM NaF] were spun down at $1000 \times g$ for 2 min at 4°C . MRC5 cells were grown at low and high density and washed with $1 \times \text{PBS}$ and lysed in ice-cold IP lysis buffer: 25 mM Tris-HCl pH 7.4, 150 mM KCl, 0.5% (v/v) NP-40, 2 mM EDTA, 1 mM NaF, cOmplete protease inhibitor cocktail (Roche), phosphatase inhibitor cocktail 2 and 3 (Sigma-Aldrich) and RNAase A. Samples were incubated on ice for 15 min and centrifuged at $17,000 \times g$ for 15 min at 4°C . Lysates was added to the washed beads and incubated overnight at 4°C with constant mixing. Tubes were spun at $1000 \times g$ for 3 min at 4°C . Beads were washed three times with 1 mL ice-cold wash buffer (25 mM Tris-HCl pH 7.4, 300 mM KCl, 0.5% (v/v) NP-40). Fifteen μL of LDS sample buffer was then added to the beads and boiled for 10 min at 95°C . Beads were collected by centrifugation at $1000 \times g$ for 2 min and SDS-PAGE was performed with the supernatant. Afterward, the gels were stained with Coomassie blue, and the corresponding band for endogenous YTHDF2 was sliced out for further SRM-quantification. The same procedure was performed using MRC5 cells that were grown at low density and treated with DMSO or Torin-1 at 250 nM for 24 h.

SRM-quantification of phosphorylated peptides

A stable isotope-labeled phosphopeptide as well as its non-phosphorylated counterpart were used as internal standards for phosphorylation stoichiometry determination of selected phosphopeptides from human YTHDF2. The following heavy peptides were synthesized as quantified SpikeTides-TQL (JPT Innovative Peptide solutions) with a $^{13}\text{C}^{15}\text{N}$ -labeled C-terminal arginine:

a) DGLNDDDFEPYLS(**phosphorylated**)PQAR, b) DGLNDDDFEPYLS PQAR.

100 fmol of each heavy peptide were spiked into the overnight in-gel tryptic digests which were otherwise processed as described above. To create an SRM (Selected Reaction Monitoring) method, the open source software Skyline (MacCoss Lab Software, Seattle, USA) was used. First, a spectral library was built from several LC-MS/MS discovery runs (DDA, data dependent analysis) on the hybrid triple quadrupole/linear ion trap instrument QTRAP4500 (SCIEX). According to their occurrence in the DDA runs, precursor charge states +2 and +3 with 5 transitions were included in the targeted method and the resulting transition list was imported into the instrument software (Analyst 1.6.1). In addition, the following parameters were set for the SRM-method: Q1 and Q3 set to unit resolution (0.7 m/z half-maximum peak width), dwell time 20 ms, cycle time < 3s. Second, a scheduled SRM method was created

in Skyline by annotating peptide retention times from the initial SRM run and setting the following parameters: cycle time: 2s, retention time window: 5 min.

The LC-MS/MS system consisted of an UltiMate 3000 RSLCnano System (Thermo Scientific, Dreieich) coupled via a NanoSprayII source (SCIEX) to a QTRAP4500. Peptides were separated on an Acclaim Pepmap100 C18 nano column (75 μm i.d.x150 mm, Thermo Fisher) with a C18 Acclaim Pepmap100 preconcentration column (100 μm i.d.x20mm, Thermo Fisher) in front. At a flow rate of 300 nL/min a 60 min linear gradient of 4%–40% acetonitrile in 0.1% formic acid was run. The resulting.wiff files of the SRM-measurements were imported into Skyline, which facilitated the quantification of endogenous phosphorylated or non-phosphorylated peptides by calculating the heavy-to-light ratios of the peak areas of the respective transitions. Relative quantification of phosphorylated peptides was performed in Excel by first calculating the absolute amount of either peptide species followed by adding up the amounts of the nonmodified peptide species and the related phosphorylated peptide species. Assuming this sum to represent 100%, it was possible to calculate the percentage of the phosphopeptide species.

Multiple sequence alignment and conservation scores

We obtained vertebrate ortholog YTHDF2 sequences from OrthoDB v12.⁵⁰ We aligned the sequences using Muscle⁵¹ with default settings via Jalview (<https://jalview.org>). From this alignment, we calculated conservation scores via a Jensen-Shannon divergence approach.⁵² We used a window size of 3, the BLOSUM62 matrix (also for background) and sequence weighting.

Sequence-based LIR prediction

We used the iLIR prediction tool³⁴ to predict candidate LIRs from the sequence of YTHDF2.

AlphaFold modeling and LIR prediction

We used AlphaFold modeling to predict potential interactions between YTHDF2 and different LC3/GABARAP proteins, and to obtain initial structural models for MD simulations.

We performed a fragment-based AlphaFold2.3 Multimer (AF2)^{53,67} screen, in which we screened overlapping fragments of YTHDF2 against all seven human LC3/GABARAP proteins (LC3Aa, LC3Ab, LC3B, LC3C, GABARAP, GABARAP L1, GABARAP L2), respectively, for binding to the LIR-docking site, following a recently developed protocol.⁵⁴ We split the wild-type (WT) and phosphomimetic (ST) YTHDF2 sequences into fragments of 16, 36, and 52 residues with an overlap of 75%. For the phosphomimetic YTHDF2 sequence, we mutated all serine and threonine residues in the WT sequence to glutamate. For each candidate LIR, we calculated the total occurrence as the sum of occurrences of individual binding modes. Those we calculated as the number of fragments containing (parts of) a motif and predicted to interact divided by the total number of fragments containing the interacting (part of the) motif.

Additionally, we used AlphaFold3 (AF3)⁵⁵ to model the interaction between GABARAP L2 and full-length YTHDF2. For this, we used the AF3 webserver with random seeds and obtained 5 models. For the MD simulations, we generated initial models with AF3. We describe the details of the modeled constructs in the section “Molecular dynamics simulations”. All predictions used the human sequences of the proteins, with their respective UniProt (<https://uniprot.org>): YTHDF2/Q9Y5A9; LC3Aa/Q9H492; LC3Ab/Q9H492-2; LC3B/Q9GZQ8; LC3C/Q9BXW4; GABARAP/O95166; GABARAP L1/Q9H0R8; GABARAP L2/P60520.

Molecular dynamics simulations

We ran two sets of MD simulations in this study: (i) simulations of candidate YTHDF2 LIR1 (as 24-residue fragment) in complex with GABARAP L2 and (ii) simulations of the C-terminal folded domain (CTD) of YTHDF2 (residues 383–579). In all simulations, we solvated the protein(s) in water and added 150 mM NaCl plus neutralizing ions. We used the charmm36m (July 2021 version) force field with charmm TIP3P water with increased hydrogen ϵ parameters.⁵⁶ We used Gromacs (versions 2023.2 and 2023.3)⁶⁸ as MD engine and followed a previously used simulation protocol⁵⁴ with minor deviations for system (i) and an extended equilibration phase for system (ii). We ran all simulations in triplicates.

We simulated a candidate YTHDF2 LIR1 construct (residues 24–47) in complex with GABARAP L2. We generated a structural model for the complex using AF3. For this prediction, we used phosphorylated S39 of YTHDF2, since it improved the quality of the interface in the model. For the simulations, we removed the phosphorylation. We capped the termini of the YTHDF2 fragment with an acetyl group at the N- and an aminomethyl group at the C terminus. For GABARAP L2, we used charged standard termini. We solvated the protein and performed an energy minimization and three equilibration steps (one in the NVT, two in the NPT ensemble) at a temperature of 310 K and a pressure of 1 bar with detailed settings as in a previous simulation protocol.⁵⁴ For the production runs, we used an integration timestep of 2 fs, and ran for 1 μs .

We simulated the YTHDF2 CTD based on a full-length AF3 model and extracted the CTD from it. We capped the N terminus with an acetyl group and used a charged standard C terminus. We solvated the protein and performed an energy-minimization until the largest force in the system was below 1000 kJ mol^{−1} nm^{−1}. Instead of three, we performed five equilibration steps: one in the NVT and four in the NPT ensemble. We set the target temperature to 310 K (NVT and NPT) and the target pressure to 1 bar (NPT only). We used a Berendsen thermostat with a characteristic time $\tau_T = 0.1$ ps for the first step. For the second step, we used a Berendsen thermostat with $\tau_T = 1.0$ ps and a Berendsen barostat with characteristic time $\tau_p = 5.0$ ps and a compressibility of $4.5 \cdot 10^{-5}$ bar^{−1}. Steps three to five used a v-rescale thermostat with $\tau_T = 1.0$ ps and a Parrinello-Rahman barostat with $\tau_p = 5.0$ ps

and a compressibility of $4.5 \cdot 10^{-5} \text{ bar}^{-1}$. We gradually decreased the spring constant of the position restraints on heavy atoms during minimization and equilibration: $1000 \text{ kJ mol}^{-1} \text{ nm}^{-1}$ during minimization and equilibration steps one and two, $500 \text{ kJ mol}^{-1} \text{ nm}^{-1}$ during step three, $100 \text{ kJ mol}^{-1} \text{ nm}^{-1}$ during step four, and no restraints during step five. We ran the five equilibration steps for 1 ns, 1 ns, 5 ns, 5 ns, and 5 ns, respectively, at timesteps of 1 fs, 1 fs, 1 fs, 2 fs, and 2 fs, respectively. For the production runs, we used the same settings as for the last equilibration step and ran for 2 μs .

To calculate root-mean-square fluctuations (RMSFs) we aligned the respective trajectories on the structure in the first frame, based on the C_{α} atoms. From the aligned trajectory we computed an average structure and aligned the trajectory on this new structure. We repeated the process iteratively until the change in RMSD of the current and previous average structure between two iterations was below a threshold of 0.0001 Å. Using the aligned trajectory from this final round we computed the RMSF. For the simulations of YTHDF2's CTD, we used the entire simulated protein as alignment reference. For the candidate LIR-GABARAPL2 systems, we aligned on GABARAP L2 and computed the candidate LIR RMSFs with respect to this reference. For all analysis, we used 1 ns time-steps of the respective trajectories.

We implemented analysis using Python 3 with the MD Analysis package.⁵⁷ Further, we used VMD⁵⁸ for analysis, structural alignments, and visualization.

Isothermal titration calorimetry (ITC)

All Isothermal titration calorimetry experiments were performed using a MicroCal VP-ITC microcalorimeter (Malvern Instruments Ltd., UK) with 1.4 mL of cell volume. ATG8s and the target peptides were dialyzed against ITC buffer (HEPES 25 mM, NaCl 150 mM, β -mercaptoethanol 5 mM, pH 7.5). Target <peptides> with a concentration of 700 μM was titrated to the fixed concentration of ATG8s (14 μM for LC3B and LC3C) or with a concentration of 1000 μM to 20 μM of GABARAPL2 in 10 μL steps with 26 injections in total and 180 s spacing time at 25°C. The reference power was set to 17 $\mu\text{Cal/s}$ and stirring speed to 307 rpm. Automated unbiased baseline calculation and curve integration was done with NITPIC.⁵⁹ Thermodynamic parameters and final binding affinity were generated by SEDPHAT⁶⁰ assuming an AB (1:1) hetero-association model. The first data point was excluded from the analysis. Final publication grade figures were generated by GUSSI.⁶¹

QUANTIFICATION AND STATISTICAL ANALYSIS

GraphPad Prism 10 was used for all statistical analyses. Student's t-test or two-way ANOVA was applied, depending on the comparison (e.g., two groups or multiple conditions). In all cases, *, **, *** and **** represent $p < 0.05$, $p < 0.01$, $p < 0.001$ and $p < 0.0001$, respectively. ns indicates not significant ($p > 0.05$). n denotes the number of independent biological replicates. Details of the statistical tests used are provided in the respective figure legends.

Supplemental information

**YTHDF proteins and m⁶A-RNA clients undergo
autophagic turnover during contact inhibition**

Hung Ho-Xuan, Astrid Bruckmann, Lautaro Natali, Cristian Prieto-Garcia, Jan F.M. Stuke, Lorene Brunello, Alexandre Vicente, Alexander Pfab, Hagen Wesseling, Sara Cano-Franco, Anshu Khatri, Simone Larivera, Pablo Sanz-Martinez, Benjamin de la Cruz-Thea, Anne-Claire Jacomin, Jan Prochazka, Regina Feederle, Volker Dötsch, Radislav Sedlacek, Gerhard Hummer, Stefanie Kaiser, Ivan Dikic, Melina M. Musri, Gunter Meister, and Alexandra Stolz

Figure S1

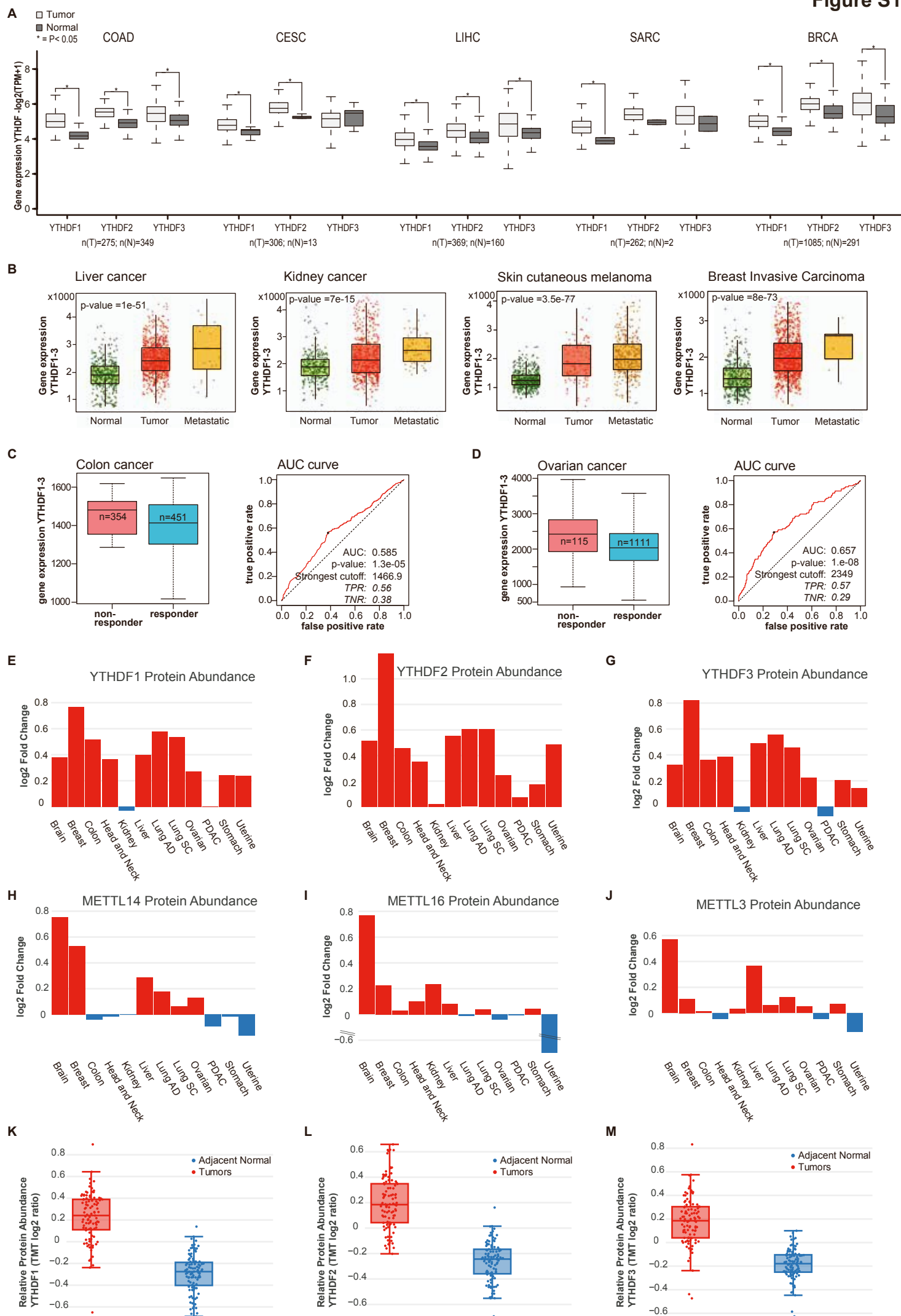


Figure S1: Gene expression signature of YTHDF protein. **A)** mRNA expression of YTHDF1, YTHDF2 and YTHDF3 genes (YTHDF1/2/3) in tumor and normal non-transformed tissue for different indicated cancer entities. Gene expression is presented as $\log_2(\text{TPM}+1)$, where TPM is transcripts per million. Gepia2 software is described previously (* $p < 0.05$) (see STAR methods). **B)** Gene expression of YTHDF signature (mean gene expression of YTHDF1-3) in normal, tumor, and metastatic samples of Liver cancer, Kidney cancer, Skin cutaneous Melanoma, and Breast Invasive Carcinoma. Data, visualization, and p-value calculation were performed by website tnmplot.com (see STAR methods). The p-value was obtained using Kruskal-Wallis test. **C,D)** Gene expression and ROC (Receiver operating characteristic) curves with AUC calculation (Area under the curve) of YTHDF signature (based on mean gene expression of YTHDF1-3) in non-responder and responder. Data, visualization, and p-value calculation were performed by website rocplot.com (see STAR methods). TPR = true positive rate; TNR = true negative rate. **E-J)** Protein expression level of indicated proteins across different tumors compared to their corresponding normal tissues. Data and visualization from the publicly available NIH database cProSite - Cancer Proteogenomic Data Analysis Site (<https://cprosite.ccr.cancer.gov/>). **K-M)** Relative protein abundance of YTHDF1, YTHDF2, and YTHDF3 in colon cancer tumors and adjacent healthy tissues. Data and visualization from the publicly available NIH database cProSite - Cancer Proteogenomic Data Analysis Site (<https://cprosite.ccr.cancer.gov/>). Unpaired p-value: < 0.0001 .

Figure S2

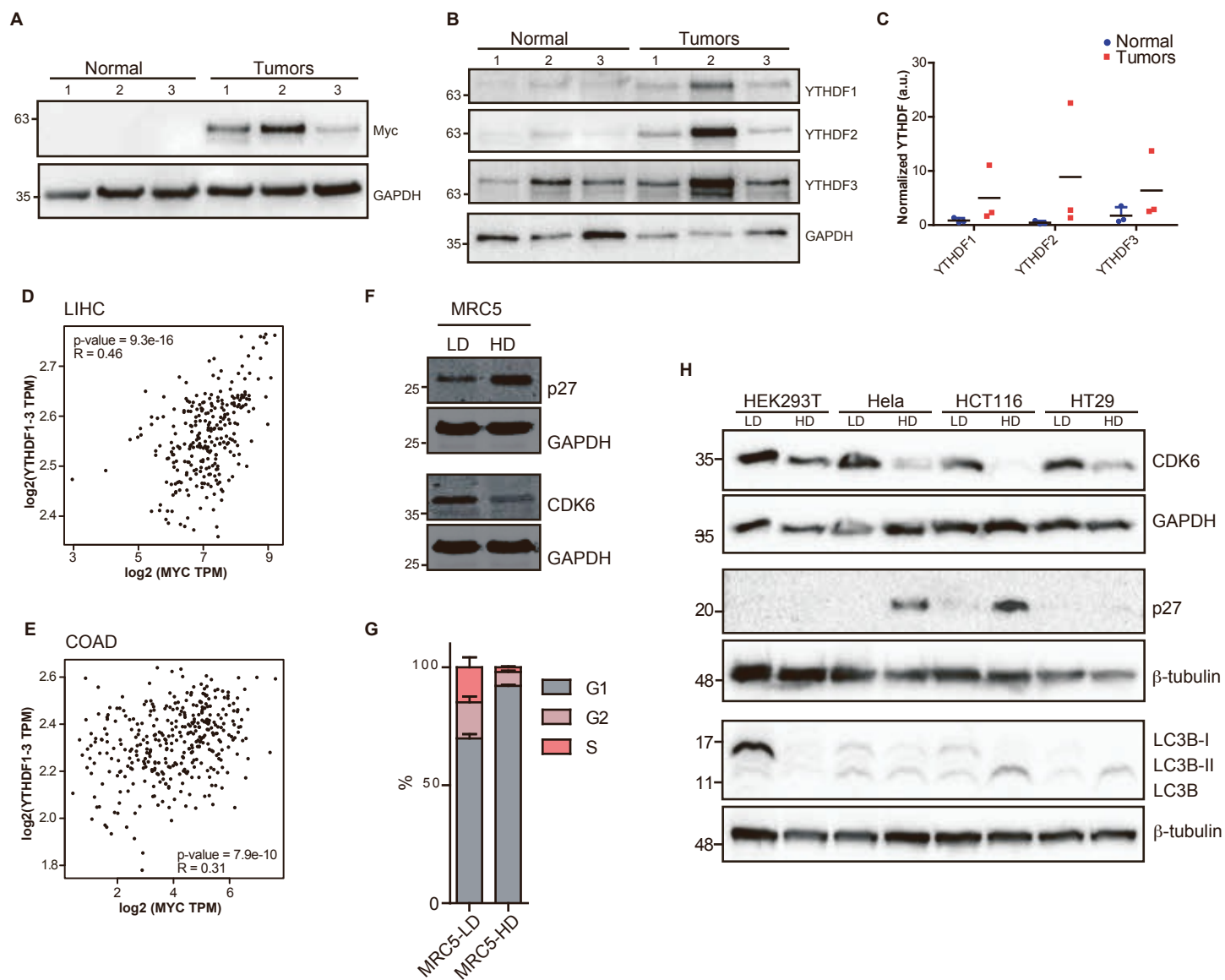


Figure S2: Correlation between expression of YTHDF protein with cMYC and expression of p27 and CDK6 in cells at low density (LD) and high density (HD). **A-B)** Western blot analysis of cMYC (**A**) and YTHDF (**B**) protein levels in primary liver tumors (Myc OE; TP53Δ) and surrounding healthy tissue from MycOE; TP53Δ liver cancer mouse model (see Star methods). n=3 mice. **C)** Quantification of B. **D, E)** correlation between MYC and YTHDF genes (1,2 and 3 together) in human Liver Hepatocellular Carcinoma (LIHC) (D) and Colon Adenocarcinoma (COAD) tumors (E). **F)** Western blot analysis of MRC5 cells harvested at LD and HD. p27 and CDK6 served as markers for cell cycle regulation. **G)** Cell cycle analysis of MRC5 cells at LD and HD. Data represents the average of three biological replicates. Error bars = SD. **H)** Western blot analysis of p27, CDK6, and LC3B from non-contact-inhibited cells (HEK293T, Hela, HCT116, HT29) cells harvested at LD and HD. GAPDH and beta-tubulin served as loading control while p27, and CDK6 served as markers for cell cycle regulation.

Figure S3

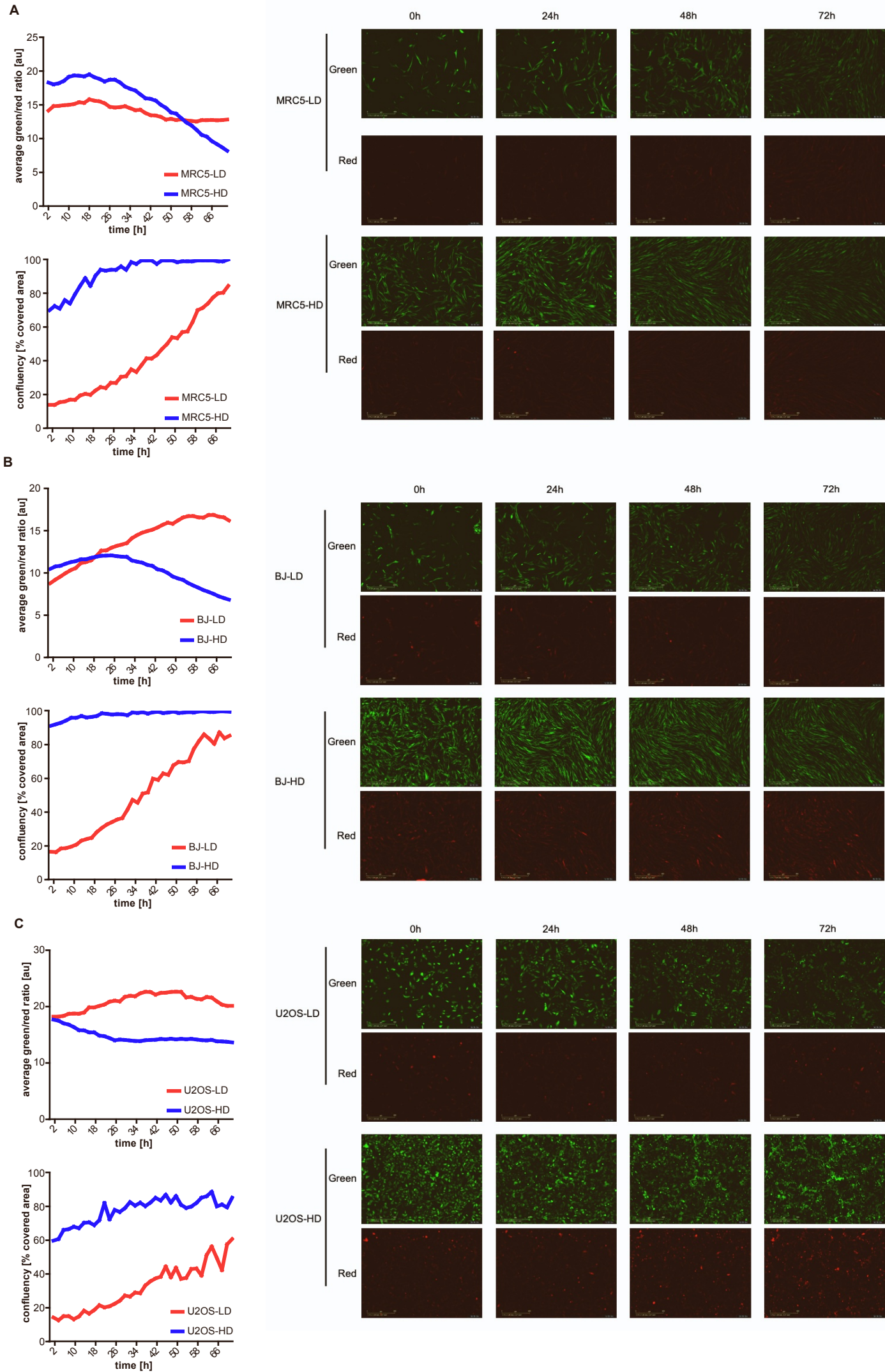


Figure S3: Autophagy flux in MRC5 and U2OS expressing the reporter EGFP-LC3-RFP-LC3 Δ G.
A-C) Autophagy flux (top left panel, low ratio=high flux), confluence (bottom left panel), and representative images (right panels) of MRC5 (**A**), BJ (**B**), and U2OS (**C**) cells stably expressing the autophagy flux reporter EGFP-LC3-RFP-LC3 Δ G and seeded at LD and HD.

Figure S4

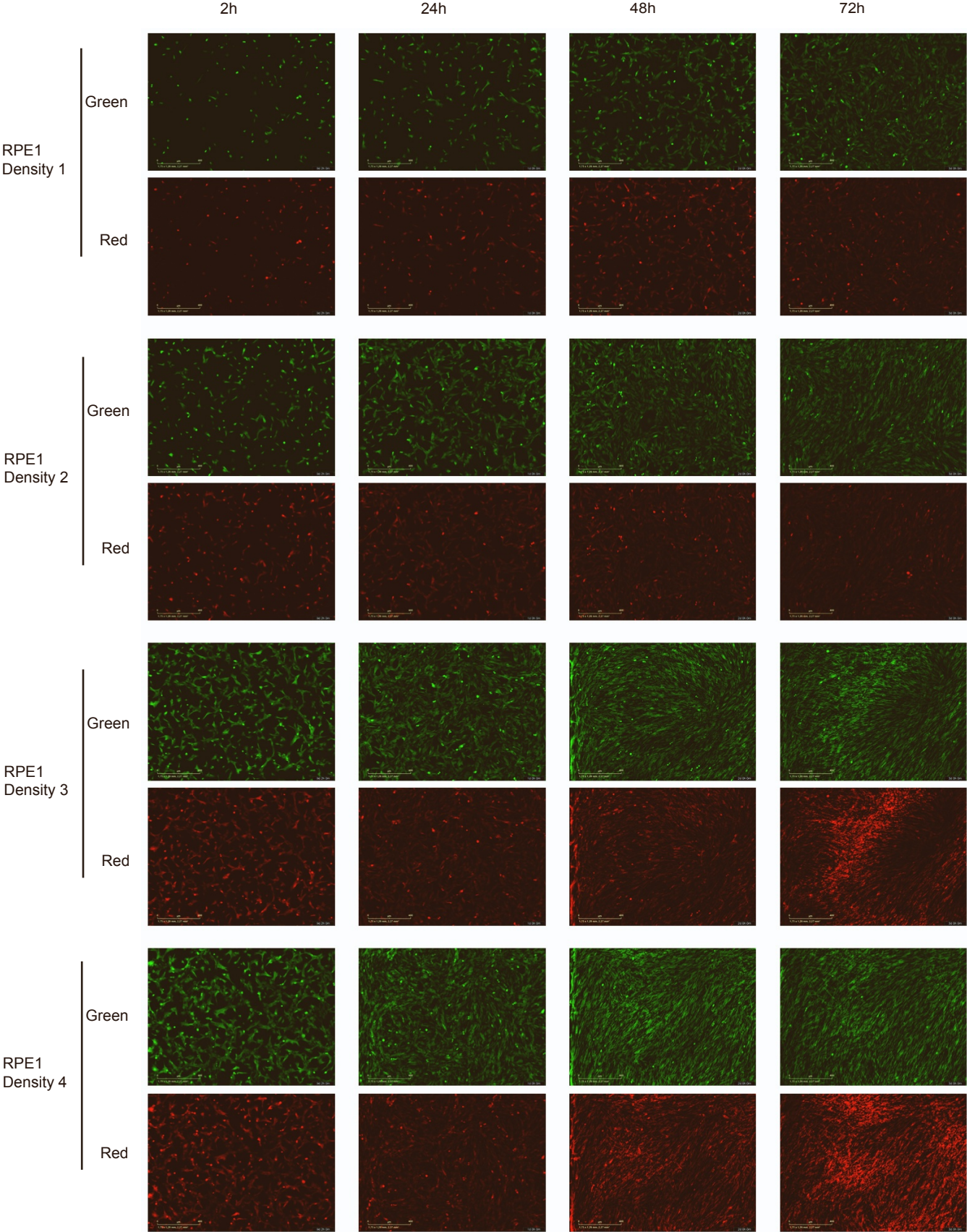


Figure S4: Autophagy flux in RPE1 cells expressing the reporter EGFP-LC3-RFP-LC3 Δ G.
Representative images of RPE1 cells expressing autophagy flux reporter EGFP-LC3-RFP-LC3 Δ G seeded at four different densities at different time points (0h, 24h, 48h, and 72h).

Figure S5

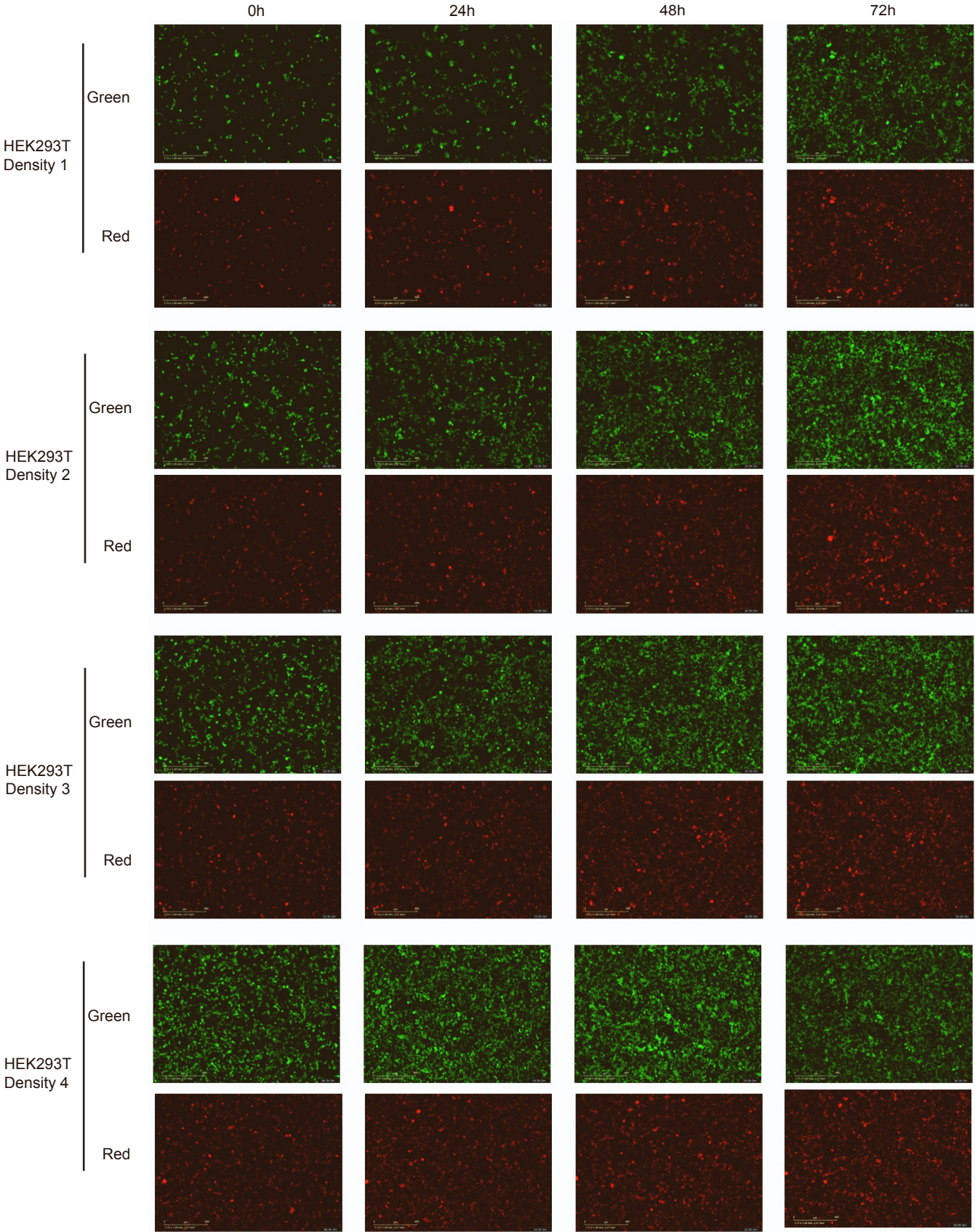


Figure S5: Autophagy flux in HEK293T cells expressing the reporter EGFP-LC3-RFP-LC3 Δ G.
Representative images of HEK293T cells expressing the autophagy flux reporter EGFP-LC3-RFP-LC3 Δ G seeded at four different densities at different time points (0h, 24h, 48h, and 72h).

Figure S6

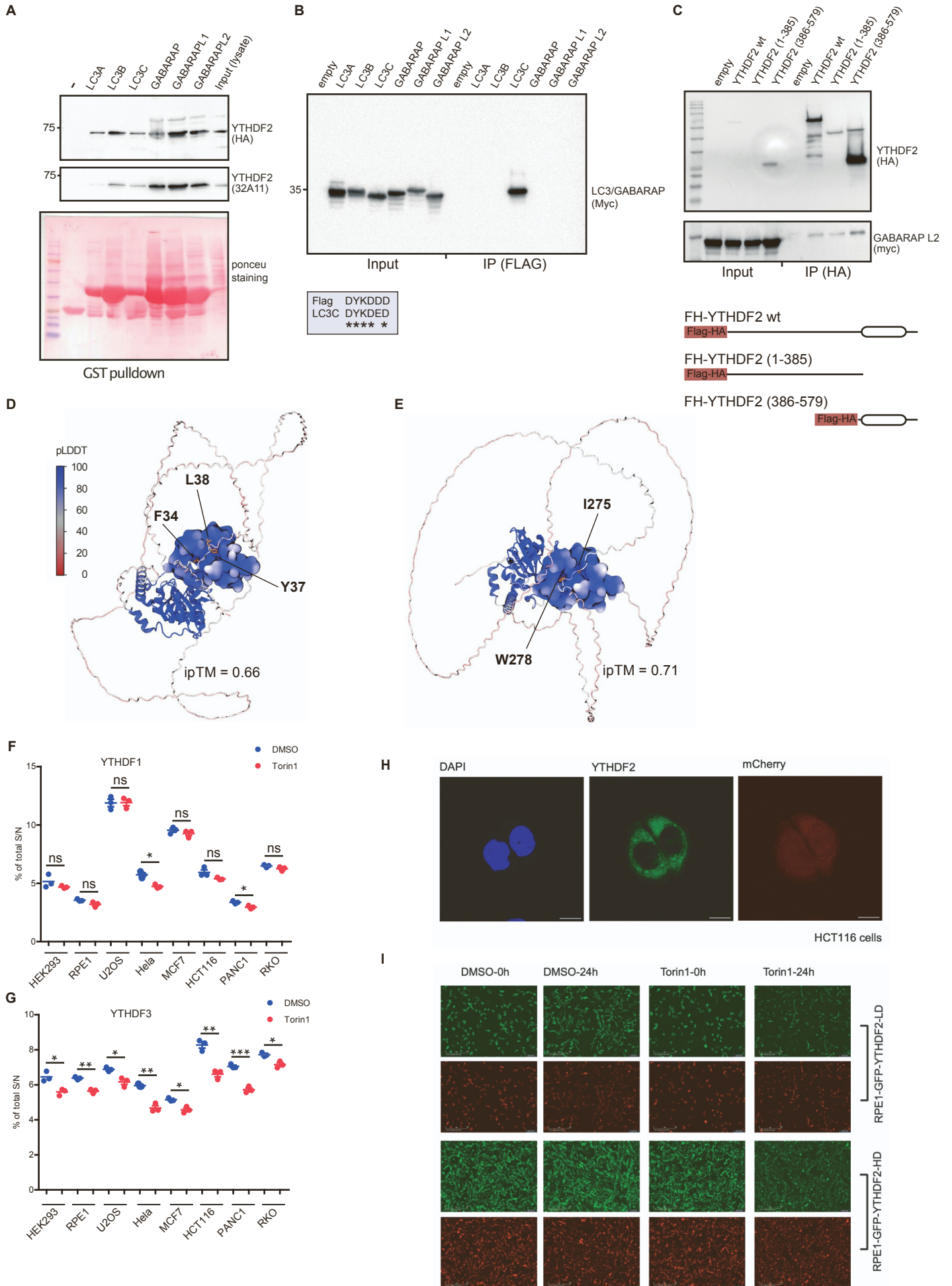


Figure S6: Binding of YTHDF2 with GABARAP L2 **A)** GST pull-down assay testing the binding of GST-tagged LC3/GABARAP with YTHDF2. **B)** Immunoprecipitation of Myc-tagged LC3/GABARAPs with only anti-Flag beads. Lower panel highlights the sequence similarity between the FLAG tag and LC3C. **C)** Lower panel: Schematic overview of YTHDF2 wt domain and the truncated versions: N terminal (YTHDF2 1-385) and C terminal (386-579) with Flag/HA tag at the N terminal. Upper panel: Co-immunoprecipitation analysis in transiently transfected HEK293T cells co-expressing Myc-tagged GABARAP L2 proteins and Flag-HA-tagged YTHDF2 wt and two truncated versions using anti-HA beads. **D-E)** AlphaFold3 predictions of GABARAP L2 and YTHDF2 suggest binding of YTHDF2 residues 34-FEPYL-37 (left) and 275-IGTW-278 (right) to GABARAP L2 in different models. YTHDF2 is shown in cartoon and GABARAP L2 in surface representation. Both are colored by pLDDT score. Residues of YTHDF2 engaging hydrophobic pockets (HPs) 1 and 2 are highlighted as orange licorice. **F-G)** Relative protein expression level of YTHDF1 (F) and YTHDF3 (G) proteins in different cell lines upon treatment with 150 nM Torin1. Data was extracted and reanalyzed from the dataset published previously [S1]. *p < 0.05, **p < 0.01, ***p < 0.001, ns (not significant). **H)** Immunofluorescent images of HCT116 cells expressing EGFP-YTHDF2 and mCherry as an internal control. **I)** Representative images of RPE1 cells expressing the autophagy flux reporter EGFP-YTHDF2-p2A-mCherry seeded at LD and HD and treated with 0.1% DMSO and 250nM Torin1 at time point 0 and 24 h after treatment.

Figure S7

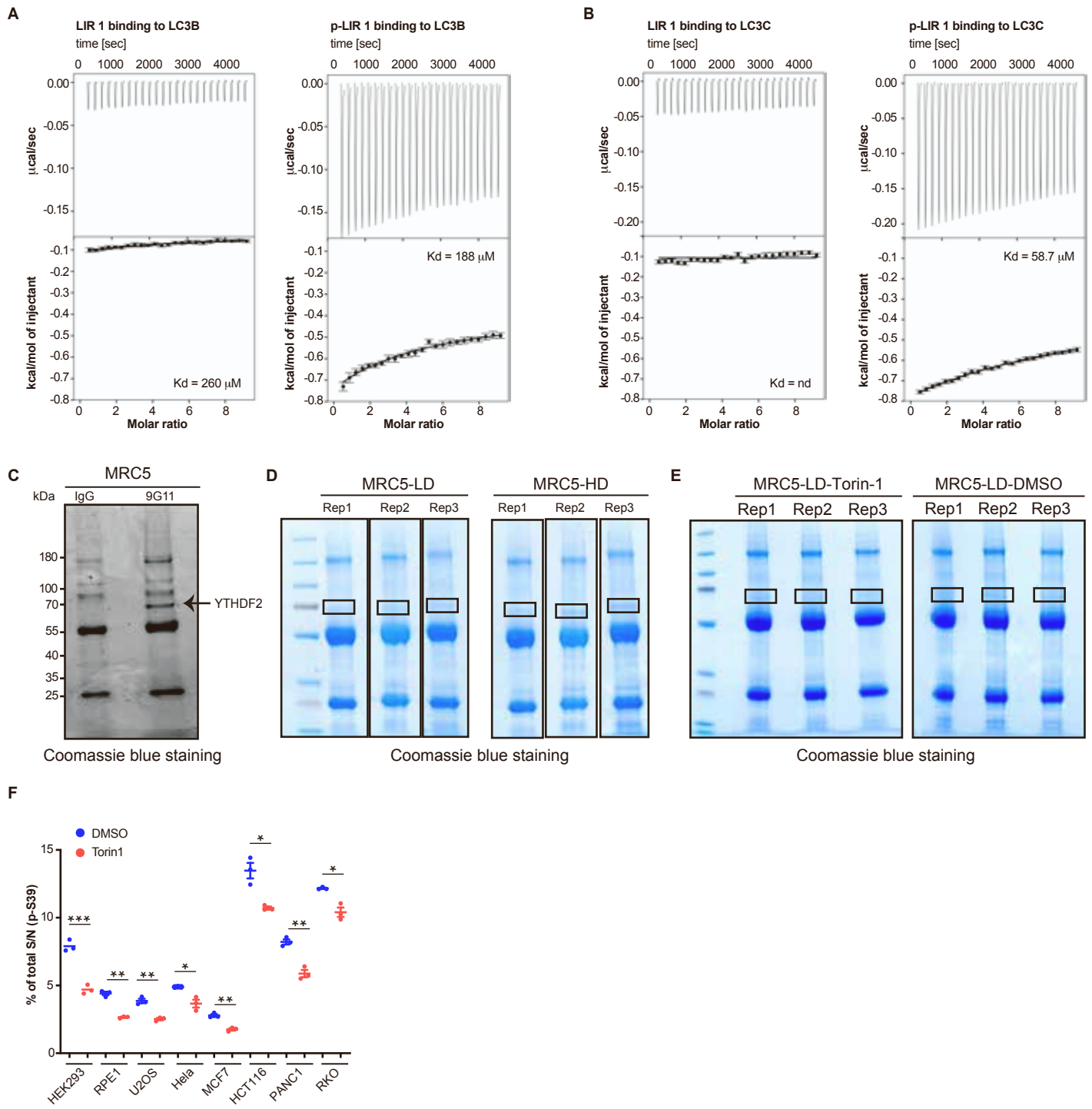


Figure S7: Interaction of LIR1 with LC3B and LC3C, and Coomassie staining of immunoprecipitation for identification of S39 phosphorylation. A-B) Interaction profile of LIR1 titrated to the members of mATG8 family (A) LC3B, (B) LC3C. Every measurement was done at 25 °C by titrating 700 μ M of peptide to 14 μ M of ATG8. The top panel of each figure shows the raw titration profile and the bottom panel displays the integrated heat of each titration event. The best fit of a single-site binding model is shown as a solid black line, generated by GUSI software. The resulting equilibrium dissociation constant (K_d) is mentioned at the bottom of every plot. **C)** Coomassie blue staining of the immunoprecipitation from MRC5 cells using IgG and anti-YTHDF2 clone 9G11. A band marked by the arrow represents YTHDF2, which is further verified by mass spectrometry. **D-E)** Coomassie blue staining of the immunoprecipitation from MRC5 cells seeded at low (LD) and high density (HD) (D) or seeded at LD and treated with 0.1% DMSO or 250nM Torin-1 (E) after immunoprecipitation with anti-YTHDF2 clone 9G11. A black box indicates the band of YTHDF2 that was sliced for targeted proteomics quantification. **F)** Relative protein expression level of S39 phosphorylation on YTHDF2 in different cell lines upon treatment with 150 nM Torin1. Data was extracted and reanalyzed from the dataset published previously [S1]. Data represent mean with standard deviation (SD). Statistics analysis was calculated using Student's *t*-test (* $p < 0.05$, ** $p < 0.01$) by GraphPad Prism 10.

Figure S8

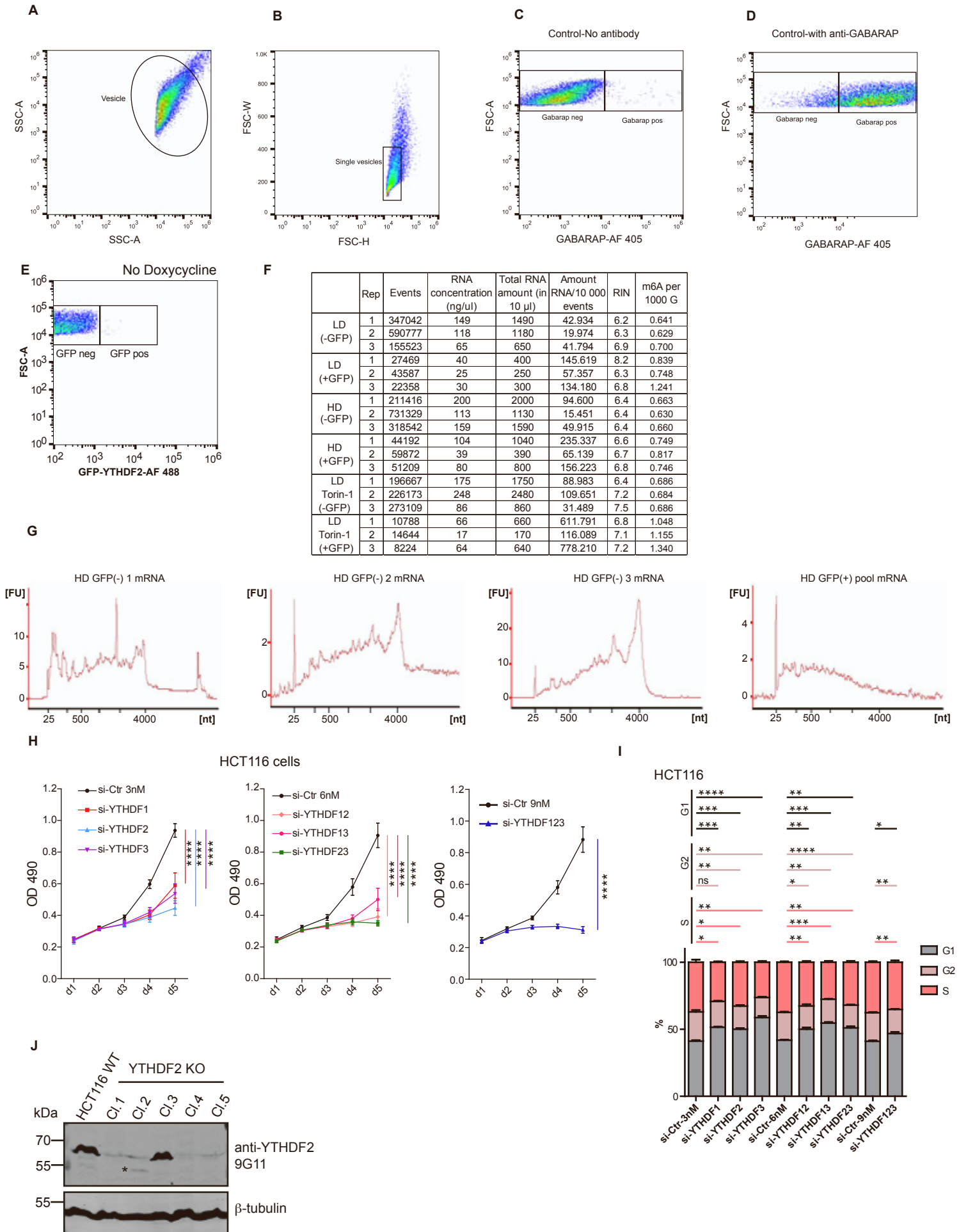


Figure S8: Establishment of FACS-based autophagosome isolation and characterization of YTHDF depletion. A-E) Scatterplot from FACS analysis showing the steps of autophagosome isolation. Panels show selection of vesicle population (A), single vesicle population (B), selection of autophagosomes without antibody control (C) with anti-GABARAP (D), and gating of GFP-negative and GFP-positive autophagosomes without doxycycline treatment (E). **F)** Table summarizing information related to RNA content of autophagosomes isolated from GFP-negative and GFP-positive autophagosomes of RPE1 cells expressing EGFP-YTHDF2-p2A-mCherry cultured in LD, HD and LD treated with 250nM of Torin1. **G)** Bioanalyzer electrophoresis of mRNA isolated from GFP-negative and GFP-positive autophagosomes of RPE1 cells expressing EGFP-YTHDF2-p2A-mCherry cultured in HD. **H)** HCT116 cells were seeded in 96-well plates, and XTT assays of the effect of YTHDF protein knockdown on cell proliferation were performed over five days. n=3; error bars=SD Statistics analysis was calculated using two-way ANOVA (****p < 0.0001) by GraphPad Prism 10. **I)** Cell cycle analysis of HCT116 upon knockdown of YTHDF proteins two days after transfection. n=3; error bars=SD. Statistics analysis was calculated using Student's *t*-test by GraphPad Prism 10. . *p < 0.05, **p < 0.01, ***p < 0.001, ****p < 0.0001, ns (not significant). **J)** Western blot of different CRISPR/Cas9-mediated knockout clones of YTHDF2 in HCT116.Luc cell lines

Supplemental reference list

[S1]. Li, J., Van Vranken, J.G., Pontano Vaite, L., Schweppe, D.K., Huttlin, E.L., Etienne, C., Nandhikonda, P., Viner, R., Robitaille, A.M., Thompson, A.H., et al. (2020). TMTpro reagents: a set of isobaric labeling mass tags enables simultaneous proteome-wide measurements across 16 samples. *Nat. Methods* 17, 399–404. 10.1038/s41592-020-0781-4.